

Crystallography, Morphology, Electronic Structure, and Transport in Non-Fullerene/Non-Indacenodithienothiophene Polymer:Y6 Solar Cells

Weigang Zhu, Austin P. Spencer, Subhrangsu Mukherjee, Joaquin M. Alzola, Vinod K. Sangwan, Samuel H. Amsterdam, Steven M. Swick, Leighton O. Jones, Michael C. Heiber, Andrew A. Herzing, Guoping Li, Charlotte L. Stern, Dean M. DeLongchamp,* Kevin L. Kohlstedt,* Mark C. Hersam,* George C. Schatz,* Michael R. Wasielewski,* Lin X. Chen,* Antonio Facchetti,* and Tobin J. Marks*



Cite This: *J. Am. Chem. Soc.* 2020, 142, 14532–14547



Read Online

ACCESS |



Metrics & More

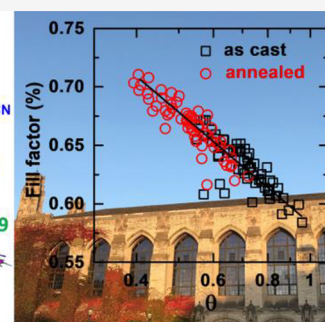
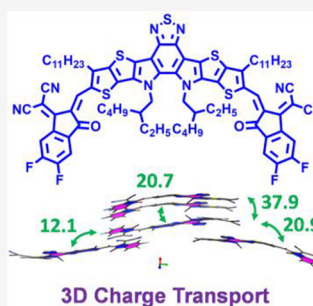


Article Recommendations



Supporting Information

ABSTRACT: Emerging nonfullerene acceptors (NFAs) with crystalline domains enable high-performance bulk heterojunction (BHJ) solar cells. Thermal annealing is known to enhance the BHJ photoactive layer morphology and performance. However, the microscopic mechanism of annealing-induced performance enhancement is poorly understood in emerging NFAs, especially regarding competing factors. Here, optimized thermal annealing of model system **PBDB-TF:Y6** (**Y6** = 2,2'-(2,2'Z)-((12,13-bis(2-ethylhexyl)-3,9-diundecyl-12,13-dihydro-[1,2,5]thiadiazolo[3,4-*e*]-thieno[2'',3'':4',5']thieno[2',3':4,5]pyrrolo[3,2-*g*]thieno[2',3':4,5]-thieno[3,2-*b*]indole-2,10-diyl)bis(methanylylidene))-bis(5,6-difluoro-3-oxo-2,3-dihydro-1*H*-indene-2,1-diylidene))dimalononitrile) decreases the open circuit voltage (V_{OC}) but increases the short circuit current (J_{SC}) and fill factor (FF) such that the resulting power conversion efficiency (PCE) increases from 14 to 15% in the ambient environment. Here we systematically investigate these thermal annealing effects through in-depth characterizations of carrier mobility, film morphology, charge photogeneration, and recombination using SCLC, GIXRD, AFM, XPS, NEXAFS, R-SoXS, TEM, STEM, fs/ns TA spectroscopy, 2DES, and impedance spectroscopy. Surprisingly, thermal annealing does not alter the film crystallinity, R-SoXS characteristic size scale, relative average phase purity, or TEM-imaged phase separation but rather facilitates **Y6** migration to the BHJ film top surface, changes the **PBDB-TF/Y6** vertical phase separation and intermixing, and reduces the bottom surface roughness. While these morphology changes increase bimolecular recombination (BR) and lower the free charge (FC) yield, they also increase the average electron and hole mobility by at least 2-fold. Importantly, the increased μ_h dominates and underlies the increased FF and PCE. Single-crystal X-ray diffraction reveals that **Y6** molecules cofacially pack via their end groups/cores, with the shortest π - π distance as close as 3.34 Å, clarifying out-of-plane π -face-on molecular orientation in the nanocrystalline BHJ domains. DFT analysis of **Y6** crystals reveals hole/electron reorganization energies of as low as 160/150 meV, large intermolecular electronic coupling integrals of 12.1–37.9 meV rationalizing the 3D electron transport, and relatively high μ_e of 10^{-4} cm² V⁻¹ s⁻¹. Taken together, this work clarifies the richness of thermal annealing effects in high-efficiency NFA solar cells and tasks for future materials design.



1. INTRODUCTION

Solar energy is one of the most powerful renewable energy resources that can be efficiently harvested by abiotic electronic devices, e.g., solar cells. Polymer solar cells (PSCs),¹ based on bulk heterojunctions (BHJs) of donor polymeric semiconductors and small-molecule acceptor materials as the photoactive layer between two metal/metal oxide electrodes, are beginning to show power conversion efficiencies (PCEs) comparable to those of commercial inorganic solar cells.^{2,3} Compared to inorganic semiconductors, organic BHJ materials are low-cost, mechanically flexible, lightweight, nontoxic, and solution-processable.^{4,5} PSCs also offer wide structural

tunability via “green” synthetic methodologies such as tin-free direct C–H arylation polymerization (DARP),^{6,7} thus attracting both fundamental scientific and technological attention.⁸ Traditionally, fullerene acceptors have dominated the PSC literature, and major advances were limited to donor

Received: May 28, 2020

Published: July 23, 2020



polymers.^{9,10} Furthermore, fullerenes are expensive, difficult to modify chemically, absorb only high-energy light, and form unstable BHJ morphologies with unstable device performance.¹¹ However, the advent of new nonfullerene acceptors (NFAs), such as indacenodithienothiophene (IDTT) acceptors, has changed this picture and enabled significantly higher PCEs than fullerenes for reasons that are not well-understood.¹² Even more remarkable, the recent emergence of the crescent-shaped acceptor 2,20-((2Z,20Z)-((12,13-bis(2-ethylhexyl)-3,9-diundecyl-12,13-dihydro-[1,2,5]-thiadiazolo[3,4-*e*]-thieno[2,3'-:4',50]thieno-[20,30:4,5]pyrrolo-[3,2]thieno-[20,30:4,5]thieno-[3,2-*b*]indole-2,10-diyl)bis(methanilylidene))bis(5,6-difluoro-3-oxo-2,3-dihydro-1*H*-indene-2,1-diylidene))dimalononitrile (Y6) (Figure 1A) has advanced PSC

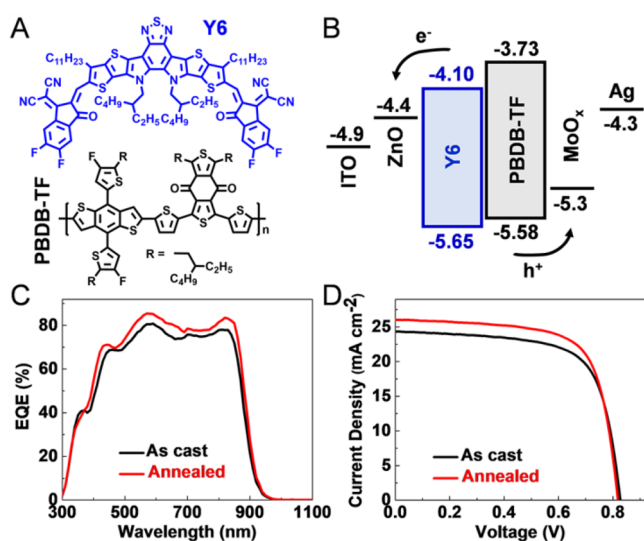


Figure 1. Materials system and solar cell performance. (A) Structures of Y6 and PBDB-TF. (B) Inverted PSC architecture and energetics. (C) EQE spectra and (D) *J*-*V* response of as-cast and thermally annealed champion PBDB-TF:Y6 solar cells.

lab PCE metrics to as high as 17.32%,^{13,14} while an in-depth structure-based model for high performance is still not clear with only sparse, largely empirical literature accounts.^{15–22} The current Y6-related research focus has largely been on developing new donor polymers,^{15,17,23} preparing Y6 variants,¹⁶ optimizing interfacial layers,²⁴ and creating ternary blends^{25,26} in the quest for higher PCEs. In parallel, there are significant efforts to develop eco-compatible processing²⁷ compatible with roll-to-roll device production.²⁸ Thus, a fundamental understanding of the reasons that Y6 enables such high PCEs should shed light on further NFA design, provide rational modification guidelines for emerging material cores, and facilitate the development of scalable processing. Compared to previous-generation ITICs, which exhibit good light absorption, high electron mobility in the ambient environment,^{12,29} low internal reorganization energies,³⁰ rapid hole transfer to polymer donors,³¹ and superior PSC operational durability,⁷ the emerging Y6 acceptors are less investigated with fewer reports of structure-based mechanistic understanding.¹⁸

Interfacial layer engineering³² and photoactive layer processing³³ play key roles in optimizing PSC performance. Typical BHJ cells are fabricated by spin-coating a polymer and an acceptor blend, while the empirical use of solvent, solvent

additives, and thermal annealing is ubiquitous. Traditionally, for polymer–fullerene BHJ blends such as P3HT:PC₆₁BM, annealing enhances polymer crystallinity, results in a 2-fold increase in the dissociated charge yield, and likely contributes to enhancing *J*_{SC} and PCE.³⁴ However, in another report, P3HT:PCBM annealing dramatically reduces the bimolecular recombination (BR) rate but increases carrier mobility. The increase in mobility dominates the BR rate to increase the FF.³⁵ However, for polymer:ITIC BHJ cells such as H11:IDIC and H12:IDIC,³⁶ thermal annealing leads to stronger absorption in the $\lambda = 350$ –620 nm wavelength range and higher, more balanced mobility. Recently, thermally annealed PM6:Y6 BHJ PSCs were reported to deliver PCE near 16.9%. (Note that polymers PM6 and PBDB-TF have the same chemical structure.²¹) Using chloroform in combination with mild annealing was thought to be key to increasing the performance by balancing hole and electron mobility and optimizing film morphology. It was proposed that enhanced film texturing and proper Y6 nanomorphology are the key factors underlying the enhanced PCE. Nevertheless, a detailed analysis of competing structural, microscopic, electronic, and exciton-dynamic aspects of these issues would doubtlessly further expand our understanding of Y6 function.

Here we focus on the PBDB-TF:Y6 model system (Figure 1A). The BHJ photovoltaic performance is evaluated in an “inverted” solar cell (Section 2.1), and the charge transport perpendicular to the substrate is characterized by a single carrier diode (Section 2.2). The film morphology is fully investigated in detail by grazing incidence film 2θ X-ray diffraction (GIXRD), AFM, XPS, near-edge X-ray absorption fine structure spectroscopy (NEXAFS), resonant soft X-ray scattering (R-SoXS), TEM, and scanning transmission electron microscopy (STEM) (Sections 2.3–2.5). Theoretical analysis not only supports the experimental data on solid-state packing and morphology but also reveals reorganization energies and π – π coupling integrals in the PBDB-TF:Y6 BHJ system (Section 2.6). Furthermore, charge photogeneration and recombination dynamics are studied by femtosecond/nanosecond transient absorption (fs/ns TA) spectroscopy (Section 2.7), two-dimensional electronic spectroscopy (2DES) (Section 2.8), and *in situ* integrated photocurrent device analysis (IPDA) (Section 2.9). In contrast to a previous report,²¹ we observe only a minimal variation in BHJ texturing.

Instead it will be seen that that Y6 partially migrates to the BHJ film top surface, changing the vertical phase separation and PBDB-TF/Y6 intermixing after thermal annealing. A direct result of this change in morphology is a 10-fold increase in hole mobility that is favorable for overall efficiency (14.13%). However, the ratio of hole and electron mobilities (mismatch factor) is also increased 5-fold, counteracting the enhanced performance via increased recombination. Overall, the central message of this article is that while thermal annealing has little effect on BHJ crystallinity/order it profoundly affects carrier mobility, charge photogeneration and recombination kinetics, and solar cell metrics in a complex fashion, in the present case fortuitously increasing the overall PCE. We also report the complete single-crystal structure of Y6, which appears to be different from that reported in the previous work,²¹ revealing short cofacial π – π stacking and, in combination with electronic structure computations, low reorganization energy, strong electronic couplings, and 3D electron transport, thus clarifying the connection between BHJ morphology and carrier mobility. For the first time, we probe

Table 1. PSC and SCLC Diode Metrics of PBDB-TF:Y6 BHJs

Device type	Device parameter	PBDB-TF:Y6 As-cast	PBDB-TF:Y6 Annealed (110 °C 3 min)
Solar Cell ^a	V_{OC} (V)	0.8305 ± 0.0043 (0.8262)	0.8189 ± 0.0052 (0.8150)
	J_{SC} (mA cm ⁻²)	23.15 ± 0.71 (24.35)	24.74 ± 0.82 (26.04)
	FF (%)	68.39 ± 1.46 (68.98)	69.77 ± 0.80 (70.50)
	PCE (%)	13.15 ± 0.42 (13.88)	14.13 ± 0.38 (14.97)
	EQE (mA cm ⁻²)	23.65	25.26
Single Carrier Diode ^b	μ_h (10 ⁻⁴ cm ² V ⁻¹ s ⁻¹)	3.97 ± 2.41	22.34 ± 6.50
	μ_e (10 ⁻⁴ cm ² V ⁻¹ s ⁻¹)	2.16 ± 1.33	3.89 ± 2.42
	μ_h / μ_e	1.84	5.74

^aAn average of ≥ 11 individual devices. Values in parentheses are from the champion PSCs. ^bAverage of ≥ 6 individual devices. The \pm symbol denotes the standard deviation.

exciton dynamic processes in Y6-based PSCs ranging from ultrafast 2DES with an 8 fs instrument response time to slow competing processes detected by IPDA down to 100 Hz. Together, this study correlates the relationship among thermal annealing, film morphology, carrier dynamics, charge transport, and solar cell metrics for high-efficiency Y6 PSCs, with many implications for future material designs.

2. RESULTS AND DISCUSSION

We begin with the synthesis of donor polymer PBDB-TF having optimum molecular mass and dispersity (Scheme S1) and then integrate it with the Y6 acceptor. The effects of thermal annealing on the photovoltaic performance, charge transport, BHJ morphology, and charge photogeneration and recombination are quantified using a diverse range of experimental techniques. For the first time, Y6 molecular geometry, single-crystal solid-state packing, B3LYP-computed internal reorganization energy, and frozen density embedding-calculated intermolecular electronic couplings are elucidated. All of the experimental details are reported in the Supporting Information (SI).

2.1. Organic Semiconductors and Solar Cell Performance. Donor polymer PBDB-TF was synthesized according to the previously reported conditions.³⁷ The number-average relative molecular mass (M_n) and the dispersity (\bar{D}) estimated by gel permeation chromatography (GPC) are 16.8 kg/mol and 2.48, respectively. PBDB-TF has a cyclic voltammetry (CV)-determined highest occupied molecular orbit (HOMO) energy of -5.58 eV and a lowest unoccupied molecular orbit (LUMO) energy of -3.73 eV ($E_{LUMO} = E_g + E_{HOMO}$) using the optical band gap, E_g , from thin films (Figure 1B).³⁰ The commercially available acceptor material Y6 was used without further purification. The CV-derived HOMO and LUMO lie at -5.65 eV and -4.10 eV,¹³ respectively. These energetics promise potentially good photovoltaic performance for PBDB-TF:Y6 BHJs.

The photovoltaic performance of the PBDB-TF:Y6 system was next evaluated using “inverted” solar cell device architecture ITO/ZnO/active layer/MoO_x/Ag (Figure 1B). The ZnO interfacial layer was deposited using sol-gel methods and is responsible for electron extraction + hole blocking. The MoO_x layer was thermally deposited in vacuum and is responsible for hole extraction + electron blocking. After extensive standard optimization/screening experiments (details in Table S4), the optimal BHJ films were achieved by blending PBDB-TF and Y6 in a 1:1 mass ratio in CHCl₃ without solvent additives, while the PBDB-TF polymer concentration ($M_n = 16.8$ kg/mol, $\bar{D} = 2.48$) was fixed at 5.5 mg mL⁻¹. The as-cast PBDB-TF:Y6 films yield average $V_{OC} = 0.8305$ V, $J_{SC} = 23.15$ mA cm⁻², FF = 68.39%, and PCE = 13.15%. After the films were annealed at 110 °C for 3 min, the average V_{OC} falls to 0.8189 V, J_{SC} rises to 24.74 mA cm⁻², and FF rises to 69.77%, affording an enhanced PCE of 14.13% (Table 1). Champion PBDB-TF:Y6 under this optimized condition achieves PCE = 14.97%, $V_{OC} = 0.815$ V, $J_{SC} = 26.04$ mA cm⁻², and FF = 70.50% (Figure 1D) under ambient conditions, comparing well with a majority of the reported data.^{13,21} Annealing at 110 °C for a shorter duration (1 min) or a longer duration (>3 min) decreases PCE. Annealing at lower and higher temperatures also lowers the PCE values. External quantum efficiency (EQE) spectra of as-cast PBDB-TF:Y6 films show a broad response from 300 to 950 nm (Figure 1C), while thermal annealing increases EQE over the entire wavelength range. The EQE J_{SC} values of as-cast and annealed PBDB-TF:Y6 films are 23.65 and 25.26 mA cm⁻², respectively, consistent with the aforementioned $J-V$ results. Note that the mismatch between device parameters from $J-V$ and EQE measurements is within 5%.^{38,39} In order to investigate the operational stability of PBDB-TF:Y6 cells, we evaluated the photovoltaic parameter loss of unencapsulated inverted devices under AM 1.5G illumination and ambient conditions (Figure S6). The PCE loss is unexpectedly significant within 60 min, contrary to a previous report.²¹

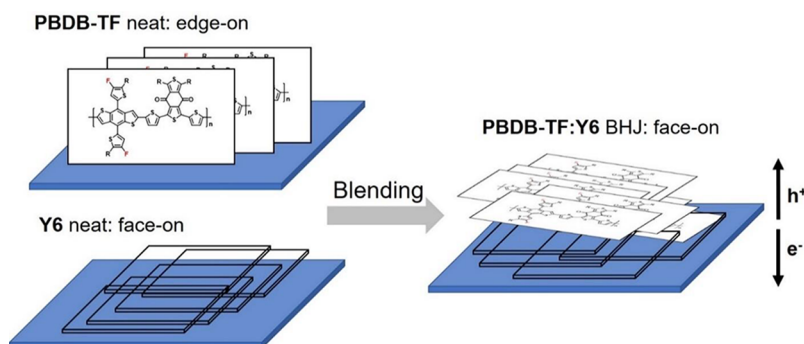


Figure 2. Crystalline packing. Schematic diagram of neat PBDB-TF (edge-on), neat Y6 (face-on) films, and PBDB-TF:Y6 BHJ film (face-on) crystalline molecular packings and orientations relative to the substrate.

The photoinstability is understandable in terms of the small domain sizes revealed by TEM (*vide infra*).

2.2. Charge-Transport Characterization. To understand the thermal annealing effect on the solar cell performance, the vertical charge transport of the neat and BHJ blend films was studied by hole-only and electron-only single carrier diode structures, ITO/MoO_x/organic/MoO_x/Ag and ITO/ZnO/organic/LiF/Al,^{30,40} respectively. In the hole-only diode, ITO/MoO_x is the hole injection electrode, and MoO_x/Ag is the hole extraction electrode, while in the electron-only diode LiF/Al is the electron injection electrode and ZnO/ITO is the electron extraction electrode. Thus, the single carrier diode structures use the same dominant interface as the “inverted” solar cell, where MoO_x/Ag is the hole extraction electrode and ZnO/ITO is the electron extraction electrode. Hole (μ_h) and electron (μ_e) mobilities were extracted in the SCLC region using a modified Mott–Gurney equation or the Murgatroyd equation (Tables 1, S6, and S7).⁴¹ The relation between current and mobility is not necessarily linear due to differences in channel length L and factor γ that accounts for trap states between different samples (Figures S7 and S8).^{30,40} The model fits the data in intermediate fields where the space charge condition ($I \sim V^2$) is satisfied. As expected, the model does not fit well in the low-field ohmic region ($I \sim V$), whereas the high-field region ($>2.5 \times 10^7$ V/m) is excluded from fitting where some diodes undergo breakdown (Figures S7 and S8). The neat polymer PBDB-TF films show $\mu_h = (3.27 \pm 1.55) \times 10^{-4}$ cm² V⁻¹ s⁻¹, similar to previous reports,^{30,42} while the neat Y6 films show $\mu_e = (2.15 \pm 0.87) \times 10^{-4}$ cm² V⁻¹ s⁻¹. The electron mobility μ_e result for Y6 films is similar to those for ITICs (10^{-5} to 10^{-4} cm² V⁻¹ s⁻¹)^{12,30,42} but lower than those of fullerenes (10^{-3} cm² V⁻¹ s⁻¹).⁴³ For comparison, as-cast PBDB-TF:Y6 films have $\mu_h = (3.97 \pm 2.41) \times 10^{-4}$ cm² V⁻¹ s⁻¹ and $\mu_e = (2.16 \pm 1.33) \times 10^{-4}$ cm² V⁻¹ s⁻¹. Annealing increases μ_h by a factor of ~ 5.6 , yielding $\mu_h = (22.34 \pm 6.50) \times 10^{-4}$ cm² V⁻¹ s⁻¹, while μ_e increases only by a factor of ~ 1.8 , yielding $\mu_e = (3.89 \pm 2.42) \times 10^{-4}$ cm² V⁻¹ s⁻¹. Note that a 5-fold increase in μ_h is observed in hole-only diodes and the μ_h improvement factor in functional BHJ cells is likely to be less than that (as suggested by IPDA measurement discussed later). As discussed below, the increased μ_h of the PBDB-TF:Y6 films after thermal annealing plausibly explains the more efficient FC (free charge) extraction (i.e., higher cell J_{SC} and FF) (Table 1); however, an increased mobility mismatch factor (μ_h/μ_e) also increases recombination.

2.3. Photoactive Layer Morphology. Next, the PBDB-TF:Y6 BHJ film morphology, microstructure, crystalline quality, and phase separation were fully investigated by

GIXRD, AFM, XPS, NEXAFS, R-SoXS, TEM, and STEM measurements. The neat PBDB-TF films exhibit only an out-of-plane (OoP) lamellar diffraction peak, corresponding to polymer chain π -edge-on packing relative to the substrate (Figures 2 and S17), similar to our previous work where chlorobenzene was used as the processing solvent³⁰ but in contrast to another report assigning both the lamellar and π - π peaks in the OoP direction.¹³ From the GIXRD experiments, PBDB-TF can be recognized as a semicrystalline polymer^{30,44} compared with amorphous polymer PBDTT-FTTE,⁴⁰ however, no DSC features are observed (Figure S3). The neat Y6 films exhibit only perfect π - π face-on stacking with $d = 3.52$ Å periodicity, in accord with the reported grazing incidence wide-angle X-ray scattering (GIWAXS) result of ~ 3.57 Å.¹³ This periodicity is consistent with the close Y6 intermolecular distances between end groups/cores that are as small as 3.3–3.4 Å in the single-crystal structure analysis (*vide infra*, Figure 5). Importantly, the mutually consistent GIXRD and single-crystal structure data for Y6 indicate that nanocrystallites are also present in the spin-coated BHJ films and that Y6 serves as a crystalline acceptor, also consistent with the DSC result showing a strong melting peak (Figure S3).

In PBDB-TF:Y6 films, the polymer PBDB-TF lamellar packing is largely suppressed due to the Y6 interaction, while the OoP π - π stacking peak is still dominant, consistent with earlier GIWAXS results.¹³ This indicates that the PBDB-TF polymer chain packing changes to a predominantly π -face-on orientation, while the Y6 molecules retain a π -face-on orientation relative to the substrate in the spin-coated PBDB-TF:Y6 films. Thus, both the polymer PBDB-TF and Y6 molecules adopt π -face-on orientations in PBDB-TF:Y6 relative to the substrate (Figure 2), as confirmed by GIXRD measurements in Figure S17, which is also a general motif that we identified previously,⁴⁵ which partially explains the observed high solar cell performance, especially the high FF (FF > 0.70; PCE > 13%). After thermal annealing at 110 °C for 3 min, the diffraction peaks and film crystallinity do not change significantly, suggesting that no additional structural ordering occurs on this annealing. This is in marked contrast with many literature reports, where thermal annealing or other processing has significant effects on film morphology and crystallinity.^{30,37,46} Specific to this blend, it was recently reported that the thermal annealing of PM6:Y6 films at 80 °C led to changes in crystal orientation and an overall increase in charge-transport balance and film crystallinity²¹ but with only a modest change in PSC performance, with PCE varying by only $\sim 1\%$ upon annealing. In contrast, the present GIXRD results

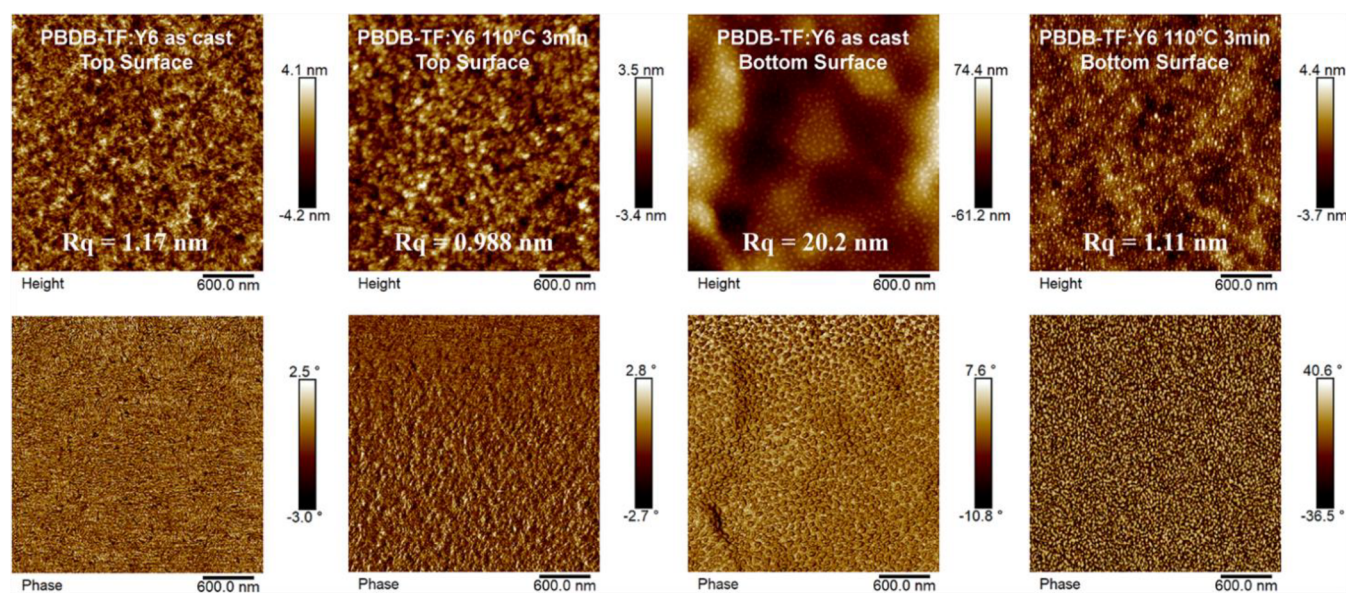


Figure 3. BHJ film morphology. AFM height and phase images of as-cast and annealed PBDB-TF:Y6 BHJ films.

Table 2. Film Morphology and Charge Dynamics Quantification of PBDB-TF:Y6 BHJs

PBDB-TF:Y6 BHJ	XPS	NEXAFS	R-SoXS		TEM	fs/ns TA
	top surface N 1s atomic ratio (%)	top surface Y6 composition (%)	characteristic size scale (nm)	relative average phase purity	Y6 domain size (nm)	k_{BR} ($\Delta A^{-1} s^{-1}$)
as-cast	2.8	31.2 ± 0.6	60	1 ± 0.01	~1 to 2	$(5.2 \pm 0.4) \times 10^8$
annealed (110 °C 3 min)	3.51	34.1 ± 0.6	60	0.96 ± 0.01	~1 to 2	$(1.7 \pm 0.1) \times 10^{10}$

show minimal correlations between carrier mobility and PSC performance metrics.

2.4. AFM and XPS Measurements. To visualize the top and bottom surface morphologies of the present films, tapping mode AFM measurements were performed under ambient conditions. The neat PBDB-TF polymer shows a randomly distributed fibrous structure, while the neat Y6 films show domain-like morphology at the top surface (Figure S10). The root-mean-square (RMS) roughness (R_q) of the neat Y6 film is ~3 nm within the $3 \mu m \times 3 \mu m$ scanned area, which is rougher than typical ITIC derivative films which are generally <1 nm within the same scan area.⁴² The rougher top surface also indicates that Y6 readily crystallizes, consistent with the GIXRD (Figure S17) and DSC results (Figure S3). For comparison, as-cast PBDB-TF:Y6 films show smooth fibrous top surfaces with $R_q = 1.17$ nm (Figure 3), corresponding to a PBDB-TF-rich component, while their bottom surface shows rough domain-like morphology ($R_q = 20.2$ nm) similar to those of neat Y6 films, corresponding to a Y6-rich component. This result suggests that the PBDB-TF:Y6 BHJ system exhibits intrinsically similar vertical semiconductor phase-separation characteristics compared to those of semicrystalline polymer:fullerene⁴⁵ and amorphous polymer:ITIC-Th systems.⁷ In this way, the PBDB-TF-rich BHJ film top surface facilitates hole extraction to the MoO_x/Ag electrode, while the Y6-rich bottom surface facilitates electron extraction to the ZnO/ITO electrode (Figure S4C), rationalizing the observed high cell J_{SC} , FF, and PCE metrics (Table 1).

After thermal annealing at 110 °C for 3 min, the PBDB-TF:Y6 films exhibit smooth top surfaces with $R_q = 0.988$ nm, a factor of ~1.2 reduction in roughness compared to those of as-cast PBDB-TF:Y6 films. Indeed, there is a change in the

mixed-domain-like and fibrous morphology. Importantly, this suggests that Y6 molecules migrate to the BHJ film top surface and change the vertical PBDB-TF/Y6 semiconductor phase separation on thermal annealing. The bottom surfaces of annealed PBDB-TF:Y6 films show similar domain-like morphologies to those of as-cast PBDB-TF:Y6 films, suggesting that Y6 is still dominant at the BHJ film bottom surface. Note that the bottom surface becomes roughly 10 times smoother after annealing at 110 °C for 3 min ($R_q = 20.2$ nm \rightarrow 1.11 nm), which should provide better electronic contact between BHJ films and cell electrodes. Both the vertical PBDB-TF/Y6 phase-separation change and better bottom electrode contact should render hole injection and bulk transport more efficient in the PBDB-TF:Y6 film, while having a small effect on electron injection, transport, and extraction (Figure S13), consistent with improved μ_h in the hole-only diodes, and improved J_{SC} , FF, PCE, and slightly depressed V_{OC} in functional BHJ cells after thermal annealing (Table 1).

XPS experiments and elemental analysis were next performed to investigate the PBDB-TF and Y6 content of the BHJ film top surface (Figures S15 and S16). The XPS of as-cast PBDB-TF:Y6 films shows an N 1s peak, suggesting that Y6 is also present in the PBDB-TF-rich top surface. The atomic ratio between N and other main elements (F, O, C, and S) is found to be 2.8% (Tables 2 and S8). In comparison, the annealed PBDB-TF:Y6 films show similar XPS results, and the N 1s atomic ratio is increased to 3.51%, which corresponds to enhanced Y6 content at the film top surface. This N 1s atomic ratio increase (2.8 \rightarrow 3.51%) correlates with the observed AFM results, where the BHJ film top surface changes dramatically from a fibrous structure to a mixed-domain-like

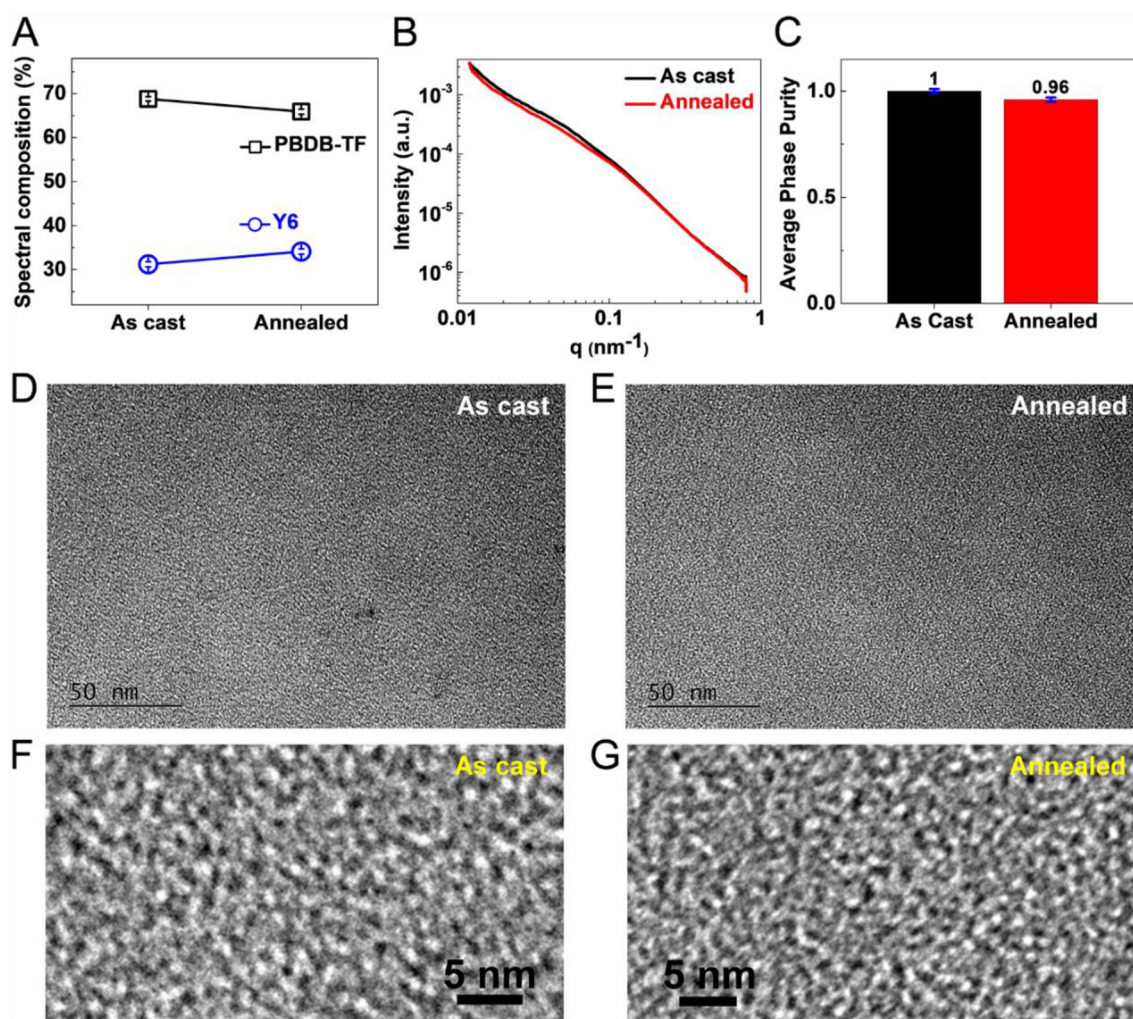


Figure 4. BHJ film morphology. (A) PBDB-TF and Y6 composition on the BHJ film top surface. (B) R-SoXS profiles. (C) Relative average phase purities from R-SoXS. Purity error bars are the standard deviation of respective values calculated from R-SoXS data at multiple energies in the range of 283 to 284 eV. TEM images of (D, F) as-cast and (E, G) annealed PBDB-TF:Y6 BHJ films. The white domains correspond to polymer PBDB-TF, while black domains correspond to small molecule Y6.

and fibrous morphology (Figure 3). The top surface is still polymer-rich (>65%, see the NEXAFS section), so Y6 migration does not dilute the polymer phase significantly and Y6 migration alone does not justify improved mobility. However, improved surface roughness at the bottom surface is likely to have a stronger effect on mobility enhancement in hole-only devices and functional cells. Mobility enhancement could also be explained by improved percolative pathways after thermal annealing that minimize the dead ends of separated charge carriers, especially holes near the electron transport layer in the bottom. Finally, Y6 is also suggested to act as an ambipolar charge-transport layer, so Y6 could also facilitate hole transport near the top surface.⁴⁷

2.5. NEXAFS and R-SoXS Experiments. To further quantify the PBDB-TF:Y6 BHJ top surface composition, NEXAFS experiments were performed. The top surface compositions extracted from the magic angle NEXAFS spectra are shown in Figure 4A. The top surfaces of both as-cast and annealed PBDB-TF:Y6 samples are found to be polymer-rich, similar to those of polymer:ITIC-Th BHJs,⁷ which is favorable for inverted solar cell structures where the top surface is used for the hole extraction. Interestingly, the Y6 content is found to

increase slightly from 31.2(6) to 34.1(6)% (Table 2) after thermal annealing, in accord with the AFM and XPS results.

Next, domain size distributions and relative average phase purities of the PBDB-TF:Y6 films were obtained with R-SoXS. R-SoXS profiles for the as-cast and annealed PBDB-TF:Y6 samples acquired at a high material contrast energy (283.8 eV) are shown in Figure 4B. Note that the selection of a proper energy for this blend is essential to probing phase separation. Indeed, the above GIXRD and NEXAFS analyses show that Y6 has a strong face-on orientation. The R-SoXS orientation contrast peaks at the π^* resonance at optimized energy for a system that is as strongly oriented as Y6 will dominate the material contrast at those energies. Furthermore, fluorescence can also be an issue. Thus, the energy of 285 eV as used recently to investigate this blend²¹ may not provide correct conclusions.

The profile shapes, peak positions, and characteristic size scales extracted from the peak positions (~ 60 nm) for the two samples are similar (Table 2). The integrated scattering intensity (ISI) of the scattering profiles reveals that the relative phase purity averaged over the measured size scales, which is proportional to \sqrt{ISI} , of the blends is also similar (Figure 4C). This result agrees with the identical degree of crystallinity from

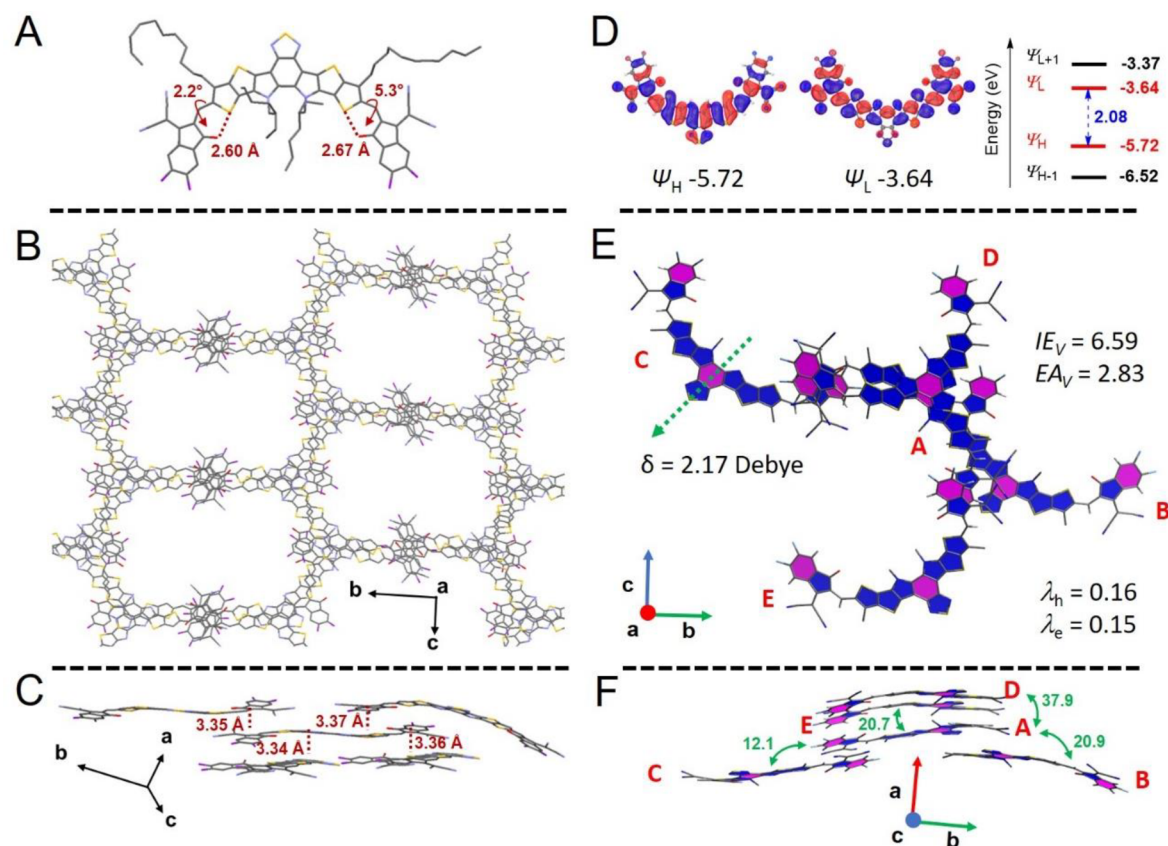


Figure 5. Single-crystal packing and DFT computations. (A) S...O distances and end-group-core torsions. (B) Crystal packing viewed along the *a* crystallographic axis. (C) π - π interactions. (D) Frontier molecular orbitals (FMOs). (E) Dipole (Debye), vertical ionization energy, vertical electron affinity and the hole/electron reorganization energies (eV). (F) Side view with electronic coupling between reference structure A and nearest neighbors B-E (meV).

GIXRD, suggesting similar semiconductor domain phase separation and ordering in as-cast and annealed PBDB-TF:Y6 samples. Note that a previous study on PM6:Y6 cells reported R-SoXS analysis performed at an unoptimized energy of 285 eV, and no correlation length fit was provided.²¹

The bulk phase separation in the PBDB-TF:Y6 films was further investigated by TEM in bright field mode.⁴⁸ The typical TEM images of as-cast (Figure 4D,F) and annealed (Figure 4E,G) PBDB-TF:Y6 films are similar, indicating no significant change after thermal annealing. The black domains correspond to Y6 due to its greater electron density, and the domain size is found to be 1 to 2 nm (Table 2), which is much smaller than reported previously for PM6:Y6 films (~10 nm)²¹ as well as in films such as PC₇₁BM (~10 nm) in PBDTT-FTTE:PC₇₁BM,⁶ ITIC (5–10) nm in polymer:ITIC,³¹ and Ph(PDI)₃ (~3.5 nm) in PBDTTT-FTTE:Ph(PDI)₃.⁴⁰ Such a small domain size spatially increases the polymer/Y6 contacting area, facilitates charge separation efficiency,⁴⁹ and rationalizes the high PCE values, agreeing with the viewpoint we proposed in 2019⁷ that smaller and well-blended BHJ domains correlate with enhanced solar cell metrics. The small domain size of Y6 also allows it to easily migrate into BHJ matrixes (thickness ~100 nm) under annealing. From the GIXRD, R-SoXS, and TEM results, the similar Y6 domain size, molecular orientation, and crystallinity in as-cast and annealed PBDB-TF:Y6 films correlate with their similar μ_e values (Table 1).

2.6. Solid-State Packing, Reorganization Energies, and Intermolecular Electronic Couplings. Single-crystal analysis of acceptor semiconductors provides insights into

intrinsic electronic couplings, charge-transport properties, and solar cell photoactive layer film morphology assignments.³⁰ To obtain a nearly complete picture of film morphology and intrinsic charge transport, single-crystal X-ray diffraction is the only experiment which can provide this information. Currently, there is minimal Y6 single crystal data reported in the literature;^{13,18,19} here we grew crystals using a solvent diffusion method (details in the SI). Y6 crystallizes in a monoclinic unit cell in a planar conformation with end-group core torsions of 5.27 and 2.23° and corresponding S–O interaction distances of 2.67 and 2.60 Å (Figure 5A). In addition, Y6 packs in a grid-like fashion, with each Y6 molecule forming very tight cofacial π - π interactions (3.35, 3.34, 3.37, and 3.36 Å) between the end groups/cores of the molecules (Figure 5C), suggesting facile electron transport through the Y6 end groups, similar to our previous findings for the ITN³⁰ and ITIC-nF⁴² NFA family. These short π - π interactions are also reflected in the GIXRD results (Figure S17), where Y6 molecules show π -face-on packing relative to the substrate in neat and blend films. The short π - π distances and grid-like packing of the Y6 single crystal should result in strong and fairly isotropic electronic transport. We will quantify the crystal transport kinetics by quantifying the electronic coupling and reorganization energies along different crystallographic directions (vide infra).

Figure 5D shows that the DFT-computed molecular orbital densities are located on the donor/acceptor segments of the HOMO (−5.72 eV) and LUMO orbitals (−3.64 eV), respectively; that of the HOMO is in excellent agreement with cyclic voltammetry ($\Delta E \approx 0.07$ eV), while the LUMO is

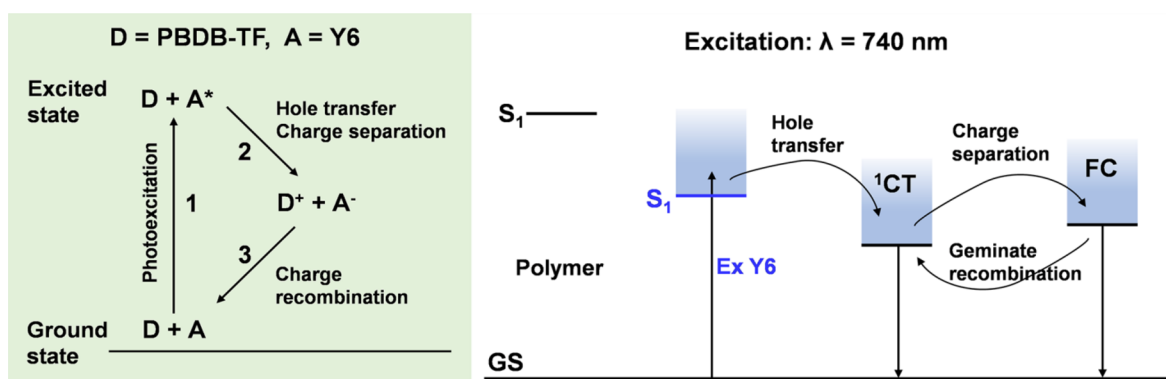


Figure 6. Photophysics model. Proposed photophysical process in the current PBDB-TF:Y6 PSC system under $\lambda = 740$ nm laser excitation. D is donor polymer PBDB-TF, and A is acceptor molecule Y6. S_1 is the lowest-energy spin-singlet excited state, 1CT is the spin-singlet charge-transfer state, FC is free charge, and GS is the ground state.

slightly below. Computed electronic structure details for Y6 are shown in Figure 5E, such as the vertical ionization energies ($IE_V = 6.59$ eV), electron affinities ($EA_V = 2.83$ eV), and hole/electron reorganization energies ($\lambda_h/\lambda_e = 160/150$ meV). The low reorganization energies for both holes and electrons suggest that not only is Y6 an excellent acceptor but it could also well be an ambipolar charge-transport material. The corner areas of the Y6 crystal were analyzed, and their electronic couplings are presented in Figure 5F. We find that although their intermolecular π - π separations are relatively close ((3.34 to 3.37) Å, Figure 5C), the nature of the packing in the crystal is such that the overlap between the donor/acceptor segments of the Y6 structure is not equal. This results in the electronic coupling between the closest neighbor (D), relative to the reference (A), having an approximate facial overlap of $\sim 50\%$, and giving $|J| = 37.9$ meV, the largest of all interactions in Y6. This value approaches those of high-performing ITIC derivatives (57 meV)⁴² and crystalline PCBM (50 meV)⁵⁰ and therefore rationalizes the very good electron-transport properties of Y6 (10^{-4} cm² V⁻¹ s⁻¹) in the ambient environment. The smallest coupling is observed between A and C, $|J| = 12.1$ meV, due to the limited overlap which is only between the acceptor segments. The close π -face-face packing eliminates weaker lateral H-bonding or van der Waals interactions and ensures good coupling and thus efficient charge transport across a Y6 domain. The strong electronic couplings between all neighbors foretell three-dimensional (3D) electron transport in Y6, very different from our previous observations of 1D or 2D charge transport in ITNs.³⁰ Another feature revealed by the DFT analysis is the large molecular dipole (Figure 5E) of 2.17 D, arising from the curved structure of Y6, which may be relevant for nonlinear optical (NLO) properties.

2.7. fs/ns Transient Absorption Spectroscopy. Next, femtosecond/nanosecond transient absorption (fs/ns TA) spectroscopy was employed to investigate the thermal annealing effects on charge photogeneration and recombination dynamics in PBDB-TF:Y6 films. Specifically, we investigated relaxation processes via a detailed kinetic model considering singlet-singlet annihilation and bimolecular and monomolecular recombination occurring on longer time scales (nanoseconds), as well as near-infrared (NIR) transitions. The excitation of Y6 at $\lambda = 740$ nm permits the selective monitoring of charge dynamics by hole transfer (Figure 6).³¹ Each PBDB-TF:Y6 film was globally fit at selected wavelengths to a higher-

order kinetic model consisting of multiple first-order decays, a singlet-singlet annihilation (SSA) component, and a bimolecular mechanism that accounts for the recombination of unbound electrons and holes (Figures S21 and S22). The appearance of PBDB-TF ground-state bleach (GSB) features at 630 nm in both as-cast and annealed PBDB-TF:Y6 films within the instrument response function ($w < 300$ fs) is indicative of ultrafast hole transfer, a known phenomenon in high-efficiency BHJs.³¹ In these blends, the bleach features are maximized with the instrument response function, so only the decay of the polymer GSB is observed (Figure 7A,B). Unexpectedly, the fits for the annealed PBDB-TF:Y6 films (Figure S22) indicate that the kinetics are accelerated versus those of the as-cast PBDB-TF:Y6 films (Figure S21). Importantly, annealed PBDB-TF:Y6 undergoes BR more rapidly ($k_{BR} = (1.7 \pm 0.1) \times 10^{10}$ ΔA^{-1} s⁻¹) than does as-cast PBDB-TF:Y6 ($k_{BR} = (5.2 \pm 0.4) \times 10^8$ ΔA^{-1} s⁻¹). Normalized spectra at long times (~ 6 ns, Figure 7C) suggest that as-cast PBDB-TF:Y6 produces a more significant quantity of free charges (FCs), contrary to initial expectations based on PCEs (Table 1). Additionally, although both blend films display long-lived PBDB-TF and Y6 GSB features suggesting the persistence of FCs, FC recombination monitored at these features in the nsTA experiment occurs more rapidly in annealed PBDB-TF:Y6 by 10-fold (Figures S26-S27), consistent with the observations from the fsTA data. As a result, as-cast PBDB-TF:Y6 films produce an overall higher yield of FCs at times > 1 μ s (Figure 7D).

The differences in the charge-carrier dynamics of the PBDB-TF:Y6 films are better understood in conjunction with the BHJ AFM, XPS, and NEXAFS morphological data. More extensive individual component mixing in the annealed PBDB-TF:Y6 film implies an increase in interfacial contact points between the PBDB-TF donor domains and Y6 acceptor domains, which increases the possibility for FCs to recombine. Thus, the accelerated FC recombination and lower overall yield in the annealed PBDB-TF:Y6 films is plausibly due to (1) altered vertical phase segregation and increased PBDB-TF/Y6 interfacial contact and (2) significantly enhanced μ_h ($> 10^{-3}$ cm² V⁻¹ s⁻¹), both of which allow the photogenerated FCs to move easily and encounter more interfaces to suffer faster and more BR. Note the TA experiments are conducted in the absence of an external electrical bias, which is known to impact the FC dynamics as well. These observations are similar to those reported for other high-performance BHJs, in which

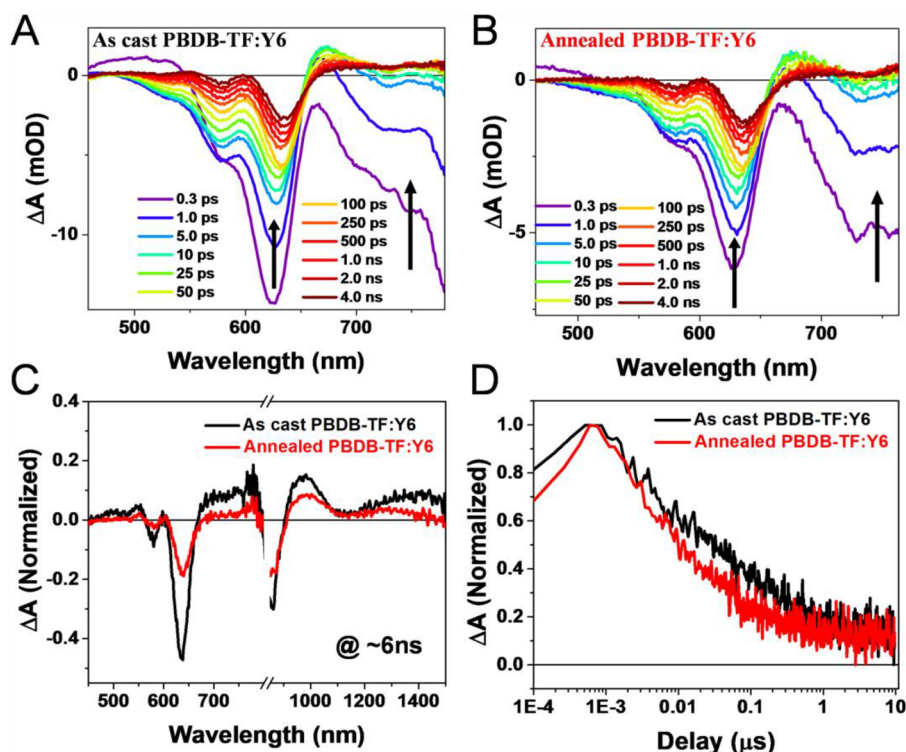


Figure 7. TA spectroscopy. (A) Selected time points of the fsTA spectrum ($\lambda_{\text{ex}} = 740$ nm) of the as-cast PBDB-TF:Y6 BHJ zoomed into the visible region demonstrating ultrafast hole transfer. (B) Selected time points of the fsTA spectrum ($\lambda_{\text{ex}} = 740$ nm) of the annealed PBDB-TF:Y6 BHJ zoomed into the visible region demonstrating ultrafast hole transfer. (C) Transient absorption spectra at 6 ns for blends excited at 740 nm in fsTA experiments, normalized to the Y6 bleach at 865 nm immediately after excitation. (D) FC decay dynamics monitored at the GSB polymer (630 nm) in the nsTA experiments.

slower/less FC recombination, longer FC lifetimes, and higher FC yields are observed in blends demonstrating clear donor/acceptor phase segregation.^{51–55} The results of this detailed ultrafast charge-transfer analysis stand in contrast to a previous PM6:Y6 study that provided ultrafast kinetics but without a kinetic model or systematic trend assessment with processing conditions.²¹ Overall, the present results suggest that the primary factors determining the increased PCE in annealed PBDB-TF:Y6 films are morphological in nature, and the ultrafast photogenerated charge-carrier dynamics are not the only factor determining the final PCE since other factors such as photon absorption, charge-carrier transport, and the current collection also affect the full photoconversion process in a complete device.^{56–58} Therefore, other electronic measurements will be needed to further quantitatively probe the origin of the PBDB-TF:Y6 PSC performance differences.

2.8. Two-Dimensional Electronic Spectroscopy. Two-dimensional electronic spectroscopy (2DES)⁵⁹ was applied for the first time in a PSC material to elucidate differences in electronic relaxation between as-cast and annealed PBDB-TF:Y6 films. Using a rapid-scanning 2DES apparatus⁶⁰ with an instrument response time of 8 fs, these measurements resolve dynamics well below the 300 fs limit of fsTA, potentially revealing the influence of annealing on ultrafast charge transfer. Samples were excited with 3 nJ pulses (9 nJ total excitation energy) spanning from 500 to 720 nm, covering the majority of the PBDB-TF polymer S_1 transition along with the blue side of the Y6 S_1 transition. Rephasing 2D spectra were measured in two distinct waiting time scans (T): one for short delays (50 fs $\leq T \leq 3$ ps in 10 fs steps) and another for long delays (1 ps $\leq T \leq 200$ ps in 1 ps steps). The real (absorptive) part of the

rephasing 2D spectrum at $T = 1$ ps for as-cast and annealed films is shown in Figure 8A,B, respectively. Although there is nearly quantitative agreement between linear absorption spectra for as-cast and annealed films, the peak shapes in the 2D spectra display clear differences. The as-cast film spectrum is predominantly positive, dominated by the ground-state bleach (GSB) and excited-state emission (ESE), and is relatively diagonally elongated and smooth. Conversely, the annealed film spectrum exhibits both positive (GSB and ESE) and negative (excited-state absorption) regions and is rounder in shape with some structure within the peak.

Beyond an overall decay of the signal amplitude with waiting time, neither sample exhibits significant spectral dynamics that would be clear signs of energy or charge-transfer processes. The short time scale 2DES data were globally modeled with a sum of three parallel exponential decays to yield decay-associated spectra (DAS) with time constants of 112.5 ± 0.3 fs, 975 ± 8 fs, and 18.2 ± 0.6 ps for the as-cast films (Figure S29) and 116.9 ± 0.3 fs, 854 ± 6 fs, and 14.9 ± 0.3 ps for the annealed films (Figure S31). Likewise, the long time scale 2DES data were globally modeled with a sum of three parallel exponential decays to yield DAS with time constants of 2.72 ± 0.01 , 26.3 ± 0.1 , and 855 ± 7 ps for the as-cast film (Figure S28) and 2.91 ± 0.01 , 29.2 ± 0.1 , and 827 ± 7 ps for the annealed film (Figure S30). Overall, relaxation dynamics for as-cast and annealed films show qualitative agreement.

To evaluate differences in coupling of vibrational modes to the electronic states for the PBDB-TF:Y6 films, the short time scale 2DES data were transformed into 3D spectra, with the additional frequency dimension ω_T resolving coherent vibrational motion during T . This is achieved by first subtracting the

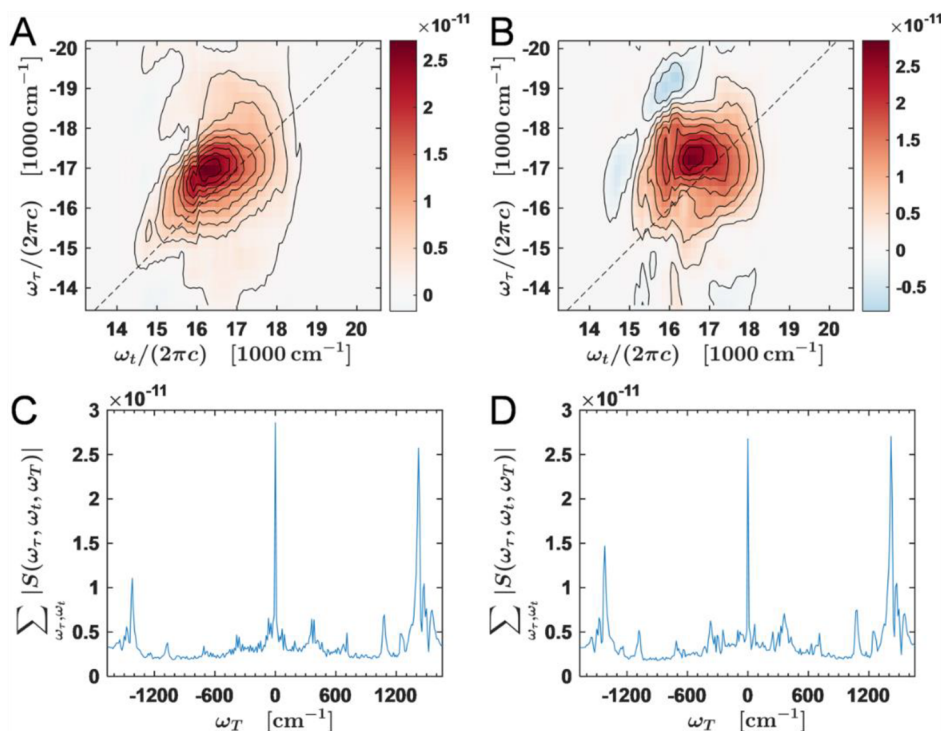


Figure 8. 2DES of PBDB-TF:Y6 films. The real-valued (absorptive) rephasing 2D spectra as a function of excitation (ω_t) and detection (ω_r) frequencies at $T = 1$ ps for (A) as-cast and (B) annealed films exhibit distinct peak shapes. Beating spectra as a function of (ω_T , generated by summing the 3D spectrum over both ω_r and ω_t) for (C) as-cast and (D) annealed films with close agreement.

decay-associated model fit from the 2D spectra (to remove incoherent relaxation dynamics) and then Fourier transforming the resulting data along the T dimension. Peaks along the ω_T dimension typically correspond to the transitions observed in resonance Raman spectroscopy, but here with added information regarding coupling to electronic transitions. Figure 8C,D shows the vibrational modes encoded in this 3D spectrum after it has been integrated over the ω_r and ω_t dimensions. In this case, both as-cast and annealed samples exhibit a broad range of coupled vibrational modes with very close agreement in vibrational frequencies and amplitudes between the two samples.

Overall, these results imply that the increase in PSC performance introduced by annealing arises not from improvements to the ultrafast steps immediately following photoexcitation but instead is isolated to slower processes that are beyond the time scales investigated here by 2DES. This can be rationalized on the basis of the observation that annealing does not significantly influence the linear absorption spectrum (an indicator of electronic structure), but instead, its impact is most apparent in the coarse morphology of the film, which is important for long-range charge transport, consistent with the observations in AFM, XPS, NEXAFS, SCLC, and fs/nsTA sections.

2.9. Integrated Photocurrent Device Analysis. Finally, we study the slower carrier recombination and extraction dynamics by analyzing *in situ* DC and impedance measurements under operating conditions. An integrated photocurrent device analysis (IPDA) is utilized to simultaneously measure all relevant device and materials parameters needed to understand the competition between recombination and extraction processes.³⁵ It is established that BHJ cell performance is limited by the BR of photogenerated carriers,

i.e., the recombination rate, $-dn/dt = k_{br} \times n^2$, where n is the carrier density and k_{br} is the bimolecular recombination coefficient.^{61–64} In optimum cells, where the active layer thickness is designed for maximum absorption, the charge extraction at the contact becomes relatively more important. In fact, a newly defined figure of merit (θ) quantifies the competition between charge recombination and extraction and reveals an inverse correlation with the FF for a wide range of organic BHJ cells with different acceptor and donor materials.⁶⁴ The competition factor is defined as

$$\theta = \frac{k_{br}GL^4}{\mu_e\mu_hV_{int}^2} \quad (1)$$

where G is the photogeneration rate, L is the thickness of the active layer, and V_{int} is the internal voltage.⁶⁴ Thus, for a high FF (i.e., small θ) high values of μ_e/μ_h and low values of k_{br} are desired while maintaining large L for efficient absorption. Different methods for measuring k_{br} and carrier mobility are known to produce significantly different values in identical cells. Uncertainties in material parameters can easily lead to conflicting conclusions on the relative importance of various mechanisms in complex BHJ systems.⁶⁵ Most transient methods, such as the open-circuit voltage decay (OCVD), for the recombination coefficient are conducted at V_{OC} and are not strictly valid at the operating point (maximum FF) of the cells.^{35,66} Charge extraction methods for mobility also suffer from extreme sensitivity to basic assumptions and result in a wide range of values depending on analysis methods.⁶⁷ Thus, the simultaneous and accurate measurement of competing material parameters is needed to understand the trade-offs in PSCs with high PCE. Such methodologies have been exploited in the BHJ systems of P3HT:PC₆₁BM and PTB7:PC₇₁BM to reveal recombination dynamics and resulting structure—

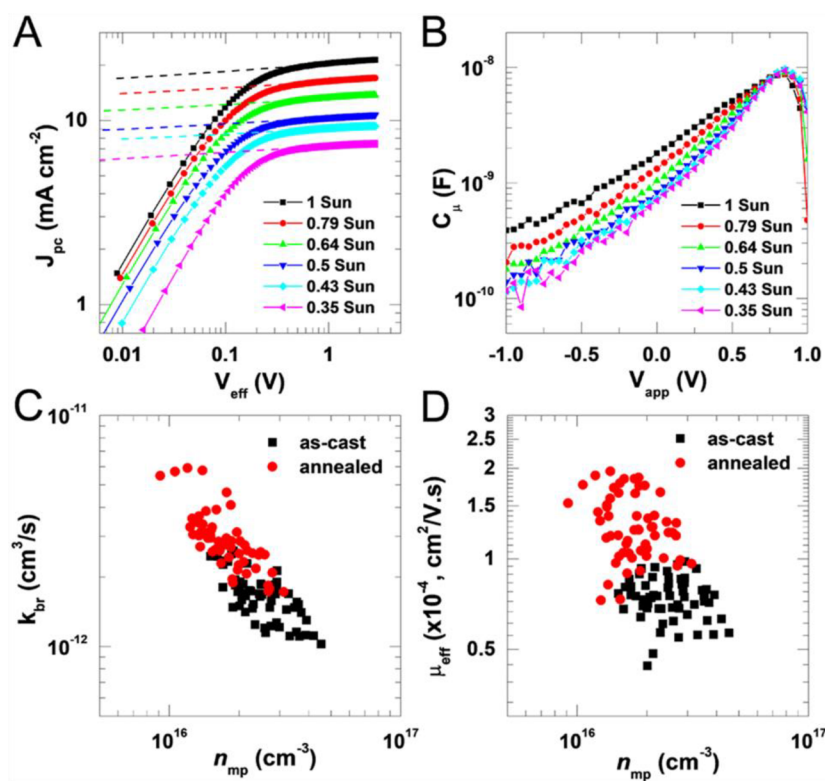


Figure 9. IPDA. (A) Plot of photocurrent versus effective voltage ($V_{\text{eff}} = V_{\text{oc}} - V$) in an annealed PBDB-TF:Y6 solar cell under varying light intensity. The dashed lines show the linear fits in the saturation regimes. Corresponding current–voltage characteristics of the cells in the dark and under illumination are shown in Figure S32. (B) Plot of chemical capacitance (C_{μ}) vs applied voltage bias (V_{app}) in an annealed PBDB-TF:Y6 solar cell under varying light intensity. (C) Plot of the bimolecular recombination coefficient (k_{br}) at the maximum power point (V_{mp}) vs carrier density (n_{mp}) at V_{mp} for 11 as-cast and 11 annealed PBDB-TF:Y6 solar cells. n_{mp} is controlled by varying the light intensity, as shown in the legends of (A) and (B). (D) Plot of effective carrier mobility (μ_{eff}) versus n_{mp} at V_{mp} for the same cells and light intensities. The other parameters extracted from the IPDA model are plotted in Figures S33 and S34.

property relationships.³⁵ However, these optimized measurement protocols have not been utilized for emerging NFA cells that are promising for next-generation solar cell technologies.^{68–70}

We conduct a comparative analysis of as-cast and annealed PBDB-TF:Y6 cells to establish correlations between material parameters such as the competition factor (θ), performance metric, and morphological changes incurred during thermal annealing. As described previously,³⁵ IPDA eliminates the most common sources of the errors by reducing the number of assumptions required to calculate the total number of carriers. Both k_{br} and effective mobility μ_{eff} (average of electron and hole mobility) can be extracted from the current–voltage (J – V) characteristics if one can extract the carrier density, $n(V)$, in the illuminated cells at all the biases. These parameters can be obtained from eqs S5 and S6, but they require the explicit calculation of $n(V)$ to obtain the recombination coefficient and mobility needed to calculate θ from eq 1. Impedance spectroscopy has been used extensively to obtain $n(V)$ in PSCs by integrating the extracted chemical capacitance, $C_{\mu}(V)$, from an equivalent RC circuit. The different approaches make different assumptions regarding the integration limits. For example, the simplest way is to assume zero carrier density at zero bias, which is not strictly accurate.^{71,72} Determining a constant value of carrier density $n_{\text{sat}}(V)$ at a chosen saturation bias (V_{sat}) results in a more accurate calculation;⁷³ however, a self-consistent calculation of $n(V)$ is expected to be even more accurate. Thus, IPDA employs a self-consistent integration

method to obtain a converged value of $n_{\text{sat}}(V)$. Moreover, the bias dependence of mobility is explicitly assumed, and the calculated values of $n(V)$ are relatively independent of the equivalent RC model assumed for the device.³⁵ The effective generation rate (J_{G}) is obtained by finding the linear regime in $J_{\text{pc}} (= J - J_{\text{dark}})$ vs $V_{\text{eff}} (= V_{\text{oc}} - V)$ plots at varying illumination intensities (Figure 9A). Figure S32 shows J – V characteristics of the same device in the dark and under 1 sun illumination. C_{μ} is obtained from the total capacitance, $C_{\text{tot}}(V)$, by $C_{\text{tot}}(V) - C_{\text{d}}(V)$, where $C_{\text{d}}(V)$ is the depletion capacitance in the dark measured at a large negative bias (–2 V) using an AC amplitude of 100 mV at 1 kHz. The resulting $C_{\mu} - V$ plot from impedance spectroscopy (Figure 9B) is used for the self-consistent calculation of $n(V)$. The data in Figure 9A,B are shown for an annealed PBDB-TF:Y6 cell with a PCE of 10.2% and an FF of 62%. Thus, k_{br} and μ_{eff} are obtained at the maximum PCE operating voltage (V_{mp}) for both as-cast and annealed PBDB-TF:Y6 solar cells, as shown in Figure 9C,D, respectively.

The FF and PCE values of all 22 measured cells are shown in Figure S33. We also extracted the Langevin prefactor or reduction factor from all measured devices (Figure S34); however, a clear effect of annealing is absent. Instead, after annealing, the PBDB-TF:Y6 cells show an increase in k_{br} and μ_{eff} values concurrent with slightly decreased total carrier densities (Figure 9C,D). Increased k_{br} after annealing is also consistent with the TA spectroscopy (*vide supra*). However, the competition factor θ ($\sim k_{\text{br}}/(\mu_{\text{eff}}^2)$) depends more strongly

on the effective mobility than on the recombination coefficient, resulting in overall decreased values of θ (Figure 10).

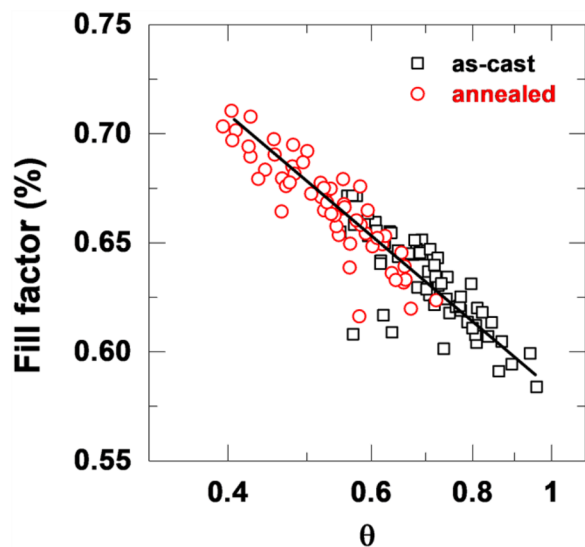


Figure 10. IPDA. Plot of FF versus θ obtained from the recombination rate to the charge extraction rate ratio for 11 cells each of the as-cast and annealed batches. Annealed cells show reduced θ and increased FF, while both kinds of cells follow similar qualitative trends.

Interestingly, data points from all as-cast and annealed PBDB-TF:Y6 devices lie on a single line of the inverse correlation between FF and θ , thus confirming the underlying BR model.^{35,64} Note that there is a shift in the absolute value of θ determined by the IPDA method as compared to that reported in ref 64 that made several assumptions to allow the extraction of θ from the vast literature. With IPDA, the competition factor is calculated by using more accurate measurements of the elements that make up eq 1, and we specifically make sure to measure each of them under maximum power operating conditions. Also, as shown by Heiber et al.,⁷⁴ many common recombination measurement techniques, e.g., the open-circuit voltage decay measurement, appear to significantly overestimate the recombination coefficient relative to what is measured by IPDA largely because they measure it at open circuit. However, IPDA shows that the dominant effect of annealing is to increase the carrier mobility, as also confirmed by the SCLC measurements in Table 1. Annealing increases the μ_h (~ 5.6 -fold in hole-only diodes) much more than μ_e (~ 1.8 -fold in electron-only diodes), and such effects are not captured in the current IPDA model since it assumes equal electron and hole mobilities and we extract effective (average) mobility. Mobility measurements in IPDA are also somewhat underestimated since PCE values decrease by ~ 10 – 15% during measurements involving extended (~ 30 min) light exposure in the ambient environment. The overall performance is limited by lower mobility carriers (electrons),⁷⁵ and the enhancement factor is consistent between SCLC and IPDA measurements. However, the overall increase in mobility produces a qualitative trend in the decreased θ and increased FF on thermal annealing.

3. CONCLUSIONS

Thermal annealing effects on the model PBDB-TF:Y6 BHJ NFA solar cell system have been characterized in depth by

performing SCLC, GIXRD, AFM, XPS, NEXAFS, R-SoXS, TEM, STEM, fs/ns TA spectroscopy, 2DES, and IPDA measurements as well as Y6 single-crystal X-ray diffraction and theoretical computations. The data and their analysis allow us to answer why and how thermal annealing changes the polymer solar cell performance metrics, which we believe are not fully understood within the PSC community, even though higher performance is reported in PSCs on thermal annealing.²¹ PBDB-TF and Y6 adopt π -face-on packing relative to the substrate in spin-coated PBDB-TF:Y6 films; unexpectedly, annealing does not change the molecular orientations, film crystallinity, R-SoXS characteristic size scales, relative average phase purities, or TEM-imaged bulk phase separation but forces Y6 vertical migration toward the BHJ film top surface, changes PBDB-TF/Y6 vertical-phase separation, reduces bottom surface roughness, and enhances the electronic contact between device electrodes. The unusual single-crystal structure of Y6 shows π -face-on packing with the shortest intermolecular distance between end groups/cores, as close as 3.3 to 3.4 Å, leading to large electronic couplings between all nearest-neighbor molecules ($|J| = (12.1 \text{ to } 37.9) \text{ meV}$), rationalizing the nanoscale π -face-on molecular stacking and good μ_e ($10^{-4} \text{ cm}^2 \text{ V}^{-1} \text{ s}^{-1}$) in spin-coated neat and BHJ films. The electron affinity of 2.83 eV implies excellent application as an electron acceptor, while both the hole ($\lambda_h = 160 \text{ meV}$) and electron ($\lambda_e = 150 \text{ meV}$) reorganization energies hold potential for ambipolar charge-transfer devices for light harvesting. We also find a significant molecular dipole in the ground state of 2.17 D, owing to the curved structure of Y6, which may yield nonlinear optical properties in future studies. All of these film morphology changes together enhance μ_h significantly but accelerate BR and lower the photogenerated FC yield. However, the effect of increased mobility dominates the overall device behavior. This results in a decreased competition factor between charge recombination and extraction after the thermal annealing step, thus enhancing FF and PCE. Overall, this integrated experimental and theoretical study finds BHJ blends of Y6 to be high-performing with appropriate thermal annealing, with implications for the design of next-generation polymer solar cell materials.

■ ASSOCIATED CONTENT

Supporting Information

The Supporting Information is available free of charge at <https://pubs.acs.org/doi/10.1021/jacs.0c05560>.

Material synthesis, UV–vis spectra, DSC, single-crystal structure, computations, PSC and SCLC device fabrication and measurements, AFM, TEM, STEM, XPS, GIXRD, R-SoXS and NEXAFS, fs/ns TA, 2DES, and IPDA (CIF)

Material synthesis, UV–vis spectra, DSC, single-crystal structure, computations, PSC and SCLC device fabrication and measurements, AFM, TEM, STEM, XPS, GIXRD, R-SoXS and NEXAFS, fs/ns TA, 2DES, and IPDA (PDF)

■ AUTHOR INFORMATION

Corresponding Authors

Dean M. DeLongchamp – Material Measurement Laboratory, National Institute of Standards and Technology (NIST), Gaithersburg, Maryland 20899, United States; Center for Hierarchical Materials Design (CHiMaD), Northwestern

University, Evanston, Illinois 60208, United States;
Email: dean.delongchamp@nist.gov

Kevin L. Kohlstedt – Department of Chemistry, Center for Light Energy Activated Redox Processes (LEAP), and Materials Research Center (MRC), Northwestern University, Evanston, Illinois 60208, United States; orcid.org/0000-0001-8045-0930; Email: kkohlstedt@northwestern.edu

Mark C. Hersam – Department of Chemistry, Center for Light Energy Activated Redox Processes (LEAP), Materials Research Center (MRC), Department of Materials Science and Engineering, Center for Hierarchical Materials Design (CHiMaD), and Department of Electrical and Computer Engineering, Northwestern University, Evanston, Illinois 60208, United States; orcid.org/0000-0003-4120-1426; Email: m-hersam@northwestern.edu

George C. Schatz – Department of Chemistry, Center for Light Energy Activated Redox Processes (LEAP), and Materials Research Center (MRC), Northwestern University, Evanston, Illinois 60208, United States; orcid.org/0000-0001-5837-4740; Email: g-schatz@northwestern.edu

Michael R. Wasielewski – Department of Chemistry, Center for Light Energy Activated Redox Processes (LEAP), Materials Research Center (MRC), and Institute for Sustainability and Energy (ISEN), Northwestern University, Evanston, Illinois 60208, United States; orcid.org/0000-0003-2920-5440; Email: m-wasielewski@northwestern.edu

Lin X. Chen – Department of Chemistry and Center for Light Energy Activated Redox Processes (LEAP), Northwestern University, Evanston, Illinois 60208, United States; Chemical Sciences and Engineering Division, Argonne National Laboratory, Lemont, Illinois 60439, United States; orcid.org/0000-0002-8450-6687; Email: l-chen@northwestern.edu

Antonio Facchetti – Department of Chemistry, Center for Light Energy Activated Redox Processes (LEAP), Materials Research Center (MRC), and Center for Hierarchical Materials Design (CHiMaD), Northwestern University, Evanston, Illinois 60208, United States; Flexterra Corporation, Skokie, Illinois 60077, United States; orcid.org/0000-0002-8175-7958; Email: a-facchetti@northwestern.edu

Tobin J. Marks – Department of Chemistry, Center for Light Energy Activated Redox Processes (LEAP), Materials Research Center (MRC), and Center for Hierarchical Materials Design (CHiMaD), Northwestern University, Evanston, Illinois 60208, United States; orcid.org/0000-0001-8771-0141; Email: t-marks@northwestern.edu

Authors

Weigang Zhu – Department of Chemistry, Northwestern University, Evanston, Illinois 60208, United States; orcid.org/0000-0002-5888-4481

Austin P. Spencer – Department of Chemistry, Northwestern University, Evanston, Illinois 60208, United States; orcid.org/0000-0003-4043-2062

Subhrangsu Mukherjee – Material Measurement Laboratory, National Institute of Standards and Technology (NIST), Gaithersburg, Maryland 20899, United States; orcid.org/0000-0002-5479-3750

Joaquin M. Alzola – Department of Chemistry and Center for Light Energy Activated Redox Processes (LEAP), Northwestern University, Evanston, Illinois 60208, United States

Vinod K. Sangwan – Center for Light Energy Activated Redox Processes (LEAP) and Department of Materials Science and

Engineering, Northwestern University, Evanston, Illinois 60208, United States; orcid.org/0000-0002-5623-5285

Samuel H. Amsterdam – Department of Chemistry, Northwestern University, Evanston, Illinois 60208, United States

Steven M. Swick – Department of Chemistry, Northwestern University, Evanston, Illinois 60208, United States

Leighton O. Jones – Department of Chemistry, Northwestern University, Evanston, Illinois 60208, United States; orcid.org/0000-0001-6657-2632

Michael C. Heiber – Material Measurement Laboratory, National Institute of Standards and Technology (NIST), Gaithersburg, Maryland 20899, United States; Center for Hierarchical Materials Design (CHiMaD), Northwestern University, Evanston, Illinois 60208, United States

Andrew A. Herzing – Material Measurement Laboratory, National Institute of Standards and Technology (NIST), Gaithersburg, Maryland 20899, United States

Guoping Li – Department of Chemistry, Northwestern University, Evanston, Illinois 60208, United States; orcid.org/0000-0002-8193-9639

Charlotte L. Stern – Department of Chemistry, Northwestern University, Evanston, Illinois 60208, United States


Complete contact information is available at:
<https://pubs.acs.org/10.1021/jacs.0c05560>

Notes

The authors declare no competing financial interest.

ACKNOWLEDGMENTS

This research was mainly supported by the Center for Light Energy Activated Redox Processes (LEAP), an Energy Frontier Research Center funded by the U.S. Department of Energy, Office of Science, Office of Basic Energy Sciences, under award DE-SC0001059 (T.J.M., project direction and advising; W.Z., devices; S.M.S., crystal growth; J.M.A., M.R.W., fs/ns optical spectroscopy; V.K.S., S.H.A., M. C. Heiber, and M. C. Hersam, IPDA; L.O.J., K.L.K., and G.C.S., theory), and the Office of Naval Research (ONR), under grant N00014012116 (G.L., GIWAXS). S.M. and D.M.D. acknowledge Award 70NANB14H012 from the U.S. Department of Commerce, National Institute of Standards and Technology as part of the Center for Hierarchical Materials Design. Polymer synthesis and characterization efforts were funded by AFOSR grant FA9550-18-1-0320 (W.Z. and A.F., devices, microscopy, X-ray, and DSC). The 2DES study (A.P.S.) was supported by NSF grant CHE-1665021 to L.X.C. L.X.C. was partially supported by Solar Energy Photochemistry program of the U. S. Department of Energy, Office of Science, Office of Basic Energy Sciences, through Argonne National Laboratory under Contract No. DE-AC02-06CH11357. This work made use of the EPIC, BioCryo, Keck-II, and/or SPID facilities of Northwestern's NUANCE Center, which received support from the Soft and Hybrid Nanotechnology Experimental (SHyNE) Resource (NSF ECCS-1542205). This work (IPDA) made use of the MatCI Facility which receives support from the MRSEC Program (NSF DMR-1720139) of the Materials Research Center at Northwestern University. We thank the Integrated Molecular Structure Education and Research Center (IMSERC) for characterization facilities supported by Northwestern University, National Science Foundation (NSF) under NSF CHE-1048773, Soft and

Hybrid Nanotechnology Experimental (SHyNE) Resource (NSF NNCI-1542205), the State of Illinois, and the International Institute for Nanotechnology (IIN). Portions of this research (S.M., D.M.D., NEXAFS, R-SoXS, A.A.H., STEM) were carried out at the 7-ID Spectroscopy Soft and Tender (SST-1) Beamline of the National Synchrotron Light Source II, a U.S. Department of Energy (DOE) Office of Science User Facility operated for the DOE Office of Science by Brookhaven National Laboratory under contract no. DE-SC0012704, and at Beamline 11.0.1.2 of the Advanced Light Source, which is supported by the Director, Office of Science, Office of Basic Energy Sciences, of the U.S. Department of Energy under contract no. DE-AC02-05CH11231. D. Fischer, C. Jaye, E. Gann (NSLS-II) and C. Wang (ALS) are acknowledged for assisting with the experiments. J.M.A., S.H.A., S.M.S., and G.L. thank the NSF for graduate research fellowships. We sincerely thank D. Zhao for drawing  and advising on figure design. W. Zhu thanks his grandmother for support.

REFERENCES

- (1) Lu, L.; Zheng, T.; Wu, Q.; Schneider, A. M.; Zhao, D.; Yu, L. Recent Advances in Bulk Heterojunction Polymer Solar Cells. *Chem. Rev.* **2015**, *115*, 12666–12731.
- (2) Green, M. A. The path to 25% silicon solar cell efficiency: History of silicon cell evolution. *Prog. Photovoltaics* **2009**, *17*, 183–189.
- (3) Cariou, R.; Benick, J.; Feldmann, F.; Höhn, O.; Hauser, H.; Beutel, P.; Razeq, N.; Wimplinger, M.; Bläsi, B.; Lackner, D.; Hermle, M.; Siefert, G.; Glunz, S. W.; Bett, A. W.; Dimroth, F. III–V-on-silicon solar cells reaching 33% photoconversion efficiency in two-terminal configuration. *Nature Energy* **2018**, *3*, 326–333.
- (4) Polman, A.; Knight, M.; Garnett, E. C.; Ehrler, B.; Sinke, W. C. Photovoltaic materials: Present efficiencies and future challenges. *Science* **2016**, *352*, No. aad4424.
- (5) Wang, G. D.; Adil, M. A.; Zhang, J. Q.; Wei, Z. X. Organic Solar Cells: Large-Area Organic Solar Cells: Material Requirements, Modular Designs, and Printing Methods. *Adv. Mater.* **2019**, *31*, No. 1970324.
- (6) Dudnik, A. S.; Aldrich, T. J.; Eastham, N. D.; Chang, R. P. H.; Facchetti, A.; Marks, T. J. Tin-Free Direct C–H Arylation Polymerization for High Photovoltaic Efficiency Conjugated Copolymers. *J. Am. Chem. Soc.* **2016**, *138*, 15699–15709.
- (7) Aldrich, T. J.; Zhu, W.; Mukherjee, S.; Richter, L. J.; Gann, E.; DeLongchamp, D. M.; Facchetti, A.; Melkonyan, F. S.; Marks, T. J. Stable Postfullerene Solar Cells via Direct C–H Arylation Polymerization. Morphology–Performance Relationships. *Chem. Mater.* **2019**, *31*, 4313–4321.
- (8) Brabec, C. J.; Gowrisanker, S.; Halls, J. J.; Laird, D.; Jia, S.; Williams, S. P. Polymer-fullerene bulk-heterojunction solar cells. *Adv. Mater.* **2010**, *22*, 3839–56.
- (9) Li, G.; Zhu, R.; Yang, Y. Polymer solar cells. *Nat. Photonics* **2012**, *6*, 153.
- (10) Nelson, J. Polymer:fullerene bulk heterojunction solar cells. *Mater. Today* **2011**, *14*, 462–470.
- (11) He, Y.; Li, Y. Fullerene derivative acceptors for high performance polymer solar cells. *Phys. Chem. Chem. Phys.* **2011**, *13*, 1970–1983.
- (12) Lin, Y.; Wang, J.; Zhang, Z. G.; Bai, H.; Li, Y.; Zhu, D.; Zhan, X. An electron acceptor challenging fullerenes for efficient polymer solar cells. *Adv. Mater.* **2015**, *27*, 1170–4.
- (13) Yuan, J.; Zhang, Y. Q.; Zhou, L. Y.; Zhang, G. C.; Yip, H. L.; Lau, T. K.; Lu, X. H.; Zhu, C.; Peng, H. J.; Johnson, P. A.; Leclerc, M.; Cao, Y.; Ullanski, J.; Li, Y. F.; Zou, Y. P. Single-Junction Organic Solar Cell with over 15% Efficiency Using Fused-Ring Acceptor with Electron-Deficient Core. *Joule* **2019**, *3*, 1140–1151.
- (14) Wang, T.; Sun, R.; Shi, M. M.; Pan, F.; Hu, Z. C.; Huang, F.; Li, Y. F.; Min, J. Solution-Processed Polymer Solar Cells with over 17% Efficiency Enabled by an Iridium Complexation Approach. *Adv. Energy Mater.* **2020**, *10*, 2000590.
- (15) Fan, B.; Zhang, D.; Li, M.; Zhong, W.; Zeng, Z.; Ying, L.; Huang, F.; Cao, Y. Achieving over 16% efficiency for single-junction organic solar cells. *Sci. China: Chem.* **2019**, *62*, 746–752.
- (16) Cui, Y.; Yao, H. F.; Zhang, J. Q.; Zhang, T.; Wang, Y. M.; Hong, L.; Xian, K. H.; Xu, B. W.; Zhang, S. Q.; Peng, J.; Wei, Z. X.; Gao, F.; Hou, J. H. Over 16% efficiency organic photovoltaic cells enabled by a chlorinated acceptor with increased open-circuit voltages. *Nat. Commun.* **2019**, *10*, 2515.
- (17) Xu, X.; Feng, K.; Bi, Z.; Ma, W.; Zhang, G.; Peng, Q. Single-Junction Polymer Solar Cells with 16.35% Efficiency Enabled by a Platinum(II) Complexation Strategy. *Adv. Mater.* **2019**, *31*, No. 1901872.
- (18) Karki, A.; Vollbrecht, J.; Dixon, A. L.; Schopp, N.; Schrock, M.; Reddy, G. N. M.; Nguyen, T. Q. Understanding the High Performance of over 15% Efficiency in Single-Junction Bulk Heterojunction Organic Solar Cells. *Adv. Mater.* **2019**, *31*, No. 1903868.
- (19) Perdigon-Toro, L.; Zhang, H. T.; Markina, A. S.; Yuan, J.; Hosseini, S. M.; Wolff, C. M.; Zuo, G. Z.; Stollerfoht, M.; Zou, Y. P.; Gao, F.; Andrienko, D.; Shoaee, S.; Neher, D. Barrierless Free Charge Generation in the High-Performance PM6:Y6 Bulk Heterojunction Non-Fullerene Solar Cell. *Adv. Mater.* **2020**, *32*, No. 1906763.
- (20) Swick, S. M.; Alzola, J. M.; Sangwan, V. K.; Amsterdam, S.; Zhu, W.; Jones, L. O.; Powers-Riggs, N.; Facchetti, A.; Kohlstedt, K. L.; Schatz, G. C.; Hersam, M. C.; Wasielewski, M. R.; Marks, T. J. Fluorinating π -Extended Molecular Acceptors Yields Highly Connected Crystal Structures and Low Reorganization Energies for Efficient Solar Cells. *Adv. Energy Mater.* **2020**, *10*, 2000635.
- (21) Zhu, L.; Zhang, M.; Zhou, G. Q.; Hao, T. Y.; Xu, J. Q.; Wang, J.; Qiu, C. Q.; Prine, N.; Ali, J.; Feng, W.; Gu, X. D.; Ma, Z. F.; Tang, Z.; Zhu, H. M.; Ying, L.; Zhang, Y. M.; Liu, F. Efficient Organic Solar Cell with 16.88% Efficiency Enabled by Refined Acceptor Crystallization and Morphology with Improved Charge Transfer and Transport Properties. *Adv. Energy Mater.* **2020**, *10*, 1904234.
- (22) Feng, L.-W.; Chen, J.; Mukherjee, S.; Sangwan, V. K.; Huang, W.; Chen, Y.; Zheng, D.; Strzalka, J. W.; Wang, G.; Hersam, M. C.; DeLongchamp, D.; Facchetti, A.; Marks, T. J. Readily Accessible Benzo[d]thiazole Polymers for Nonfullerene Solar Cells with > 16% Efficiency and Potential Pitfalls. *ACS Energy Lett.* **2020**, *5*, 1780–1787.
- (23) Li, W.; Liu, Q.; Jin, K.; Cheng, M.; Hao, F.; Wu, W.-Q.; Liu, S.; Xiao, Z.; Yang, S.; Shi, S.; Ding, L. Fused-ring phenazine building blocks for efficient copolymer donors. *Mater. Chem. Front.* **2020**, *4*, 1454–1458.
- (24) Wen, X. B.; Nowak-Krol, A.; Nagler, O.; Kraus, F.; Zhu, N.; Zheng, N.; Muller, M.; Schmidt, D.; Xie, Z. Q.; Wurthner, F. Tetrahydroxy-Perylene Bisimide Embedded in Zinc Oxide Thin Film as Electron Transporting Layer for High Performance Non-Fullerene Organic Solar Cells. *Angew. Chem., Int. Ed.* **2019**, *58*, 13051–13055.
- (25) Yu, R. N.; Yao, H. F.; Cui, Y.; Hong, L.; He, C.; Hou, J. H. Improved Charge Transport and Reduced Nonradiative Energy Loss Enable Over 16% Efficiency in Ternary Polymer Solar Cells. *Adv. Mater.* **2019**, *31*, 1902302.
- (26) Pan, M. A.; Lau, T. K.; Tang, Y. B.; Wu, Y. C.; Liu, T.; Li, K.; Chen, M. C.; Lu, X. H.; Ma, W.; Zhan, C. L. 16.7%-efficiency ternary blended organic photovoltaic cells with PCBM as the acceptor additive to increase the open-circuit voltage and phase purity. *J. Mater. Chem. A* **2019**, *7*, 20713–20722.
- (27) Hong, L.; Yao, H. F.; Wu, Z.; Cui, Y.; Zhang, T.; Xu, Y.; Yu, R. N.; Liao, Q.; Gao, B. W.; Xian, K. H.; Woo, H. Y.; Ge, Z. Y.; Hou, J. H. Eco-Compatible Solvent-Processed Organic Photovoltaic Cells with Over 16% Efficiency. *Adv. Mater.* **2019**, *31*, No. 1903441.
- (28) Yan, T. T.; Song, W.; Huang, J. M.; Peng, R. X.; Huang, L. K.; Ge, Z. Y. 16.67% Rigid and 14.06% Flexible Organic Solar Cells

Enabled by Ternary Heterojunction Strategy. *Adv. Mater.* **2019**, *31*, 1902210.

(29) Lin, Y.; Zhao, F.; He, Q.; Huo, L.; Wu, Y.; Parker, T. C.; Ma, W.; Sun, Y.; Wang, C.; Zhu, D.; Heeger, A. J.; Marder, S. R.; Zhan, X. High-Performance Electron Acceptor with Thienyl Side Chains for Organic Photovoltaics. *J. Am. Chem. Soc.* **2016**, *138*, 4955–61.

(30) (a) Swick, S. M.; Zhu, W. G.; Matta, M.; Aldrich, T. J.; Harbuzaru, A.; Navarrete, J. T. L.; Ortiz, R. P.; Kohlstedt, K. L.; Schatz, G. C.; Facchetti, A.; Melkonyan, F. S.; Marks, T. J. Closely packed, low reorganization energy pi-extended postfullerene acceptors for efficient polymer solar cells. *Proc. Natl. Acad. Sci. U. S. A.* **2018**, *115*, E8341–E8348. (b) Swick, S.; Gebraad, T.; Jones, L.; Fu, B.; Aldrich, T. J.; Kohlstedt, K. L.; Schatz, G. C.; Facchetti, A.; Marks, T. J. Building Blocks for High-Efficiency Organic Photovoltaics. Molecular, Crystal, and Electronic Characteristics of Post-Fullerene ITIC Ensembles. *ChemPhysChem* **2019**, *20*, 2608–2626.

(31) Eastham, N. D.; Logsdon, J. L.; Manley, E. F.; Aldrich, T. J.; Leonardi, M. J.; Wang, G.; Powers-Riggs, N. E.; Young, R. M.; Chen, L. X.; Wasielewski, M. R.; Melkonyan, F. S.; Chang, R. P. H.; Marks, T. J. Hole-Transfer Dependence on Blend Morphology and Energy Level Alignment in Polymer: ITIC Photovoltaic Materials. *Adv. Mater.* **2018**, *30*, 1704263.

(32) Zhou, N. J.; Kim, M. G.; Loser, S.; Smith, J.; Yoshida, H.; Guo, X. G.; Song, C.; Jin, H.; Chen, Z. H.; Yoon, S. M.; Freeman, A. J.; Chang, R. P. H.; Facchetti, A.; Marks, T. J. Amorphous oxide alloys as interfacial layers with broadly tunable electronic structures for organic photovoltaic cells. *Proc. Natl. Acad. Sci. U. S. A.* **2015**, *112*, 7897–7902.

(33) Aubry, T. J.; Ferreira, A. S.; Yee, P. Y.; Aguirre, J. C.; Hawks, S. A.; Fontana, M. T.; Schwartz, B. J.; Tolbert, S. H. Processing Methods for Obtaining a Face-On Crystalline Domain Orientation in Conjugated Polymer-Based Photovoltaics. *J. Phys. Chem. C* **2018**, *122*, 15078–15089.

(34) Clarke, T. M.; Ballantyne, A. M.; Nelson, J.; Bradley, D. D. C.; Durrant, J. R. Free Energy Control of Charge Photogeneration in Polythiophene/Fullerene Solar Cells: The Influence of Thermal Annealing on P3HT/PCBM Blends. *Adv. Funct. Mater.* **2008**, *18*, 4029–4035.

(35) Heiber, M. C.; Okubo, T.; Ko, S.-J.; Luginbuhl, B. R.; Ran, N. A.; Wang, M.; Wang, H.; Uddin, M. A.; Woo, H. Y.; Bazan, G. C.; Nguyen, T.-Q. Measuring the competition between bimolecular charge recombination and charge transport in organic solar cells under operating conditions. *Energy Environ. Sci.* **2018**, *11*, 3019–3032.

(36) Bin, H.; Yang, Y.; Zhang, Z.-G.; Ye, L.; Ghasemi, M.; Chen, S.; Zhang, Y.; Zhang, C.; Sun, C.; Xue, L.; Yang, C.; Ade, H.; Li, Y. 9.73% Efficiency Nonfullerene All Organic Small Molecule Solar Cells with Absorption-Complementary Donor and Acceptor. *J. Am. Chem. Soc.* **2017**, *139*, 5085–5094.

(37) Aldrich, T. J.; Swick, S. M.; Melkonyan, F. S.; Marks, T. J. Enhancing Indacenodithiophene Acceptor Crystallinity via Substituent Manipulation Increases Organic Solar Cell Efficiency. *Chem. Mater.* **2017**, *29*, 10294–10298.

(38) Snaith, H. J. The perils of solar cell efficiency measurements. *Nat. Photonics* **2012**, *6*, 337–340.

(39) Zimmermann, E.; Ehrenreich, P.; Pfadler, T.; Dorman, J. A.; Weickert, J.; Schmidt-Mende, L. Erroneous efficiency reports harm organic solar cell research. *Nat. Photonics* **2014**, *8*, 669–672.

(40) Zhu, W. G.; Alzola, J. M.; Aldrich, T. J.; Kohlstedt, K. L.; Zheng, D.; Hartnett, P. E.; Eastham, N.; Huang, W.; Wang, G.; Young, R. M.; Schatz, G. C.; Wasielewski, M. R.; Facchetti, A.; Melkonyan, F. S.; Marks, T. J. Fluorine Tuning of Morphology, Energy Loss, and Carrier Dynamics in Perylenediimide Polymer Solar Cells. *ACS Energy Lett.* **2019**, *4*, 2695–2702.

(41) Murgatroyd, P. N. Theory of space-charge-limited current enhanced by Frenkel effect. *J. Phys. D: Appl. Phys.* **1970**, *3*, 151–156.

(42) Aldrich, T. J.; Matta, M.; Zhu, W.; Swick, S. M.; Stern, C. L.; Schatz, G. C.; Facchetti, A.; Melkonyan, F. S.; Marks, T. J. Fluorination Effects on Indacenodithienothiophene Acceptor Packing

and Electronic Structure, End-Group Redistribution, and Solar Cell Photovoltaic Response. *J. Am. Chem. Soc.* **2019**, *141*, 3274–3287.

(43) Mihailetschi, V. D.; van Duren, J. K. J.; Blom, P. W. M.; Hummelen, J. C.; Janssen, R. A. J.; Kroon, J. M.; Rispen, M. T.; Verhees, W. J. H.; Wienk, M. M. Electron transport in a methanofullerene. *Adv. Funct. Mater.* **2003**, *13*, 43–46.

(44) Noriega, R.; Rivnay, J.; Vandewal, K.; Koch, F. P. V.; Stingelin, N.; Smith, P.; Toney, M. F.; Salleo, A. A general relationship between disorder, aggregation and charge transport in conjugated polymers. *Nat. Mater.* **2013**, *12*, 1038–1044.

(45) Guo, X.; Zhou, N.; Lou, S. J.; Smith, J.; Tice, D. B.; Hennek, J. W.; Ortiz, R. P.; Navarrete, J. T. L.; Li, S.; Strzalka, J.; Chen, L. X.; Chang, R. P. H.; Facchetti, A.; Marks, T. J. Polymer solar cells with enhanced fill factors. *Nat. Photonics* **2013**, *7*, 825–833.

(46) Li, W.; Chen, M.; Cai, J.; Spooner, E. L. K.; Zhang, H.; Gurney, R. S.; Liu, D.; Xiao, Z.; Lidzey, D. G.; Ding, L.; Wang, T. Molecular Order Control of Non-fullerene Acceptors for High-Efficiency Polymer Solar Cells. *Joule* **2019**, *3*, 819–833.

(47) Xiao, C.; Li, C.; Liu, F.; Zhang, L.; Li, W. Single-crystal field-effect transistors based on a fused-ring electron acceptor with high ambipolar mobilities. *J. Mater. Chem. C* **2020**, *8*, 5370–5374.

(48) Huang, Y.; Kramer, E. J.; Heeger, A. J.; Bazan, G. C. Bulk Heterojunction Solar Cells: Morphology and Performance Relationships. *Chem. Rev.* **2014**, *114*, 7006–7043.

(49) Gélinas, S.; Rao, A.; Kumar, A.; Smith, S. L.; Chin, A. W.; Clark, J.; van der Poll, T. S.; Bazan, G. C.; Friend, R. H. Ultrafast Long-Range Charge Separation in Organic Semiconductor Photovoltaic Diodes. *Science* **2014**, *343*, 512–516.

(50) Gajdos, F.; Oberhofer, H.; Dupuis, M.; Blumberger, J. On the Inapplicability of Electron-Hopping Models for the Organic Semiconductor Phenyl-C61-butyric Acid Methyl Ester (PCBM). *J. Phys. Chem. Lett.* **2013**, *4*, 1012–1017.

(51) Liu, T.; Huo, L.; Chandrabose, S.; Chen, K.; Han, G.; Qi, F.; Meng, X.; Xie, D.; Ma, W.; Yi, Y.; Hodgkiss, J. M.; Liu, F.; Wang, J.; Yang, C.; Sun, Y. Optimized Fibril Network Morphology by Precise Side-Chain Engineering to Achieve High-Performance Bulk-Heterojunction Organic Solar Cells. *Adv. Mater.* **2018**, *30*, 1707353.

(52) Ferron, T.; Waldrup, M.; Pope, M.; Collins, B. A. Increased charge transfer state separation via reduced mixed phase interface in polymer solar cells. *J. Mater. Chem. A* **2019**, *7*, 4536–4548.

(53) Tang, Z.; Wang, J.; Melianas, A.; Wu, Y.; Kroon, R.; Li, W.; Ma, W.; Andersson, M. R.; Ma, Z.; Cai, W.; Tress, W.; Inganäs, O. Relating open-circuit voltage losses to the active layer morphology and contact selectivity in organic solar cells. *J. Mater. Chem. A* **2018**, *6*, 12574–12581.

(54) Gao, W.; Liu, T.; Luo, Z.; Zhang, L.; Ming, R.; Zhong, C.; Ma, W.; Yan, H.; Yang, C. Regulating exciton bonding energy and bulk heterojunction morphology in organic solar cells via methyl-functionalized non-fullerene acceptors. *J. Mater. Chem. A* **2019**, *7*, 6809–6817.

(55) Zhang, J.; Li, Y.; Hu, H.; Zhang, G.; Ade, H.; Yan, H. Chlorinated Thiophene End Groups for Highly Crystalline Alkylated Non-Fullerene Acceptors toward Efficient Organic Solar Cells. *Chem. Mater.* **2019**, *31*, 6672–6676.

(56) Song, X.; Gasparini, N.; Ye, L.; Yao, H.; Hou, J.; Ade, H.; Baran, D. Controlling Blend Morphology for Ultrahigh Current Density in Nonfullerene Acceptor-Based Organic Solar Cells. *ACS Energy Lett.* **2018**, *3*, 669–676.

(57) Izawa, S.; Shintaku, N.; Hiramoto, M. Effect of Band Bending and Energy Level Alignment at the Donor/Acceptor Interface on Open-Circuit Voltage in Organic Solar Cells. *J. Phys. Chem. Lett.* **2018**, *9*, 2914–2918.

(58) Yuan, J.; Huang, T.; Cheng, P.; Zou, Y.; Zhang, H.; Yang, J. L.; Chang, S. Y.; Zhang, Z.; Huang, W.; Wang, R.; Meng, D.; Gao, F.; Yang, Y. Enabling low voltage losses and high photocurrent in fullerene-free organic photovoltaics. *Nat. Commun.* **2019**, *10*, 570.

(59) Jonas, D. M. Two-Dimensional Femtosecond Spectroscopy. *Annu. Rev. Phys. Chem.* **2003**, *54*, 425–463.

- (60) Spencer, A. P.; Chen, L. X. Rapid acquisition of broadband two-dimensional electronic spectra by continuous scanning with conventional delay lines. *Opt. Lett.* **2020**, *45*, 2942–2945.
- (61) Bartelt, J. A.; Lam, D.; Burke, T. M.; Sweetnam, S. M.; McGehee, M. D. Charge-Carrier Mobility Requirements for Bulk Heterojunction Solar Cells with High Fill Factor and External Quantum Efficiency > 90%. *Adv. Energy Mater.* **2015**, *5*, 1500577.
- (62) Nelson, J. *The Physics of Solar Cells*; Imperial College Press: 2003.
- (63) Ramirez, I.; Causa, M.; Zhong, Y.; Banerji, N.; Riede, M. Key Tradeoffs Limiting the Performance of Organic Photovoltaics. *Adv. Energy Mater.* **2018**, *8*, 1703551.
- (64) Bartesaghi, D.; Pérez, I. d. C.; Kniepert, J.; Roland, S.; Turbiez, M.; Neher, D.; Koster, L. J. A. Competition between recombination and extraction of free charges determines the fill factor of organic solar cells. *Nat. Commun.* **2015**, *6*, 7083.
- (65) Clarke, T. M.; Lungenschmied, C.; Peet, J.; Drolet, N.; Mozer, A. J. A Comparison of Five Experimental Techniques to Measure Charge Carrier Lifetime in Polymer/Fullerene Solar Cells. *Adv. Energy Mater.* **2015**, *5*, 1401345.
- (66) Kiermasch, D.; Baumann, A.; Fischer, M.; Dyakonov, V.; Tvingstedt, K. Revisiting lifetimes from transient electrical characterization of thin film solar cells; a capacitive concern evaluated for silicon, organic and perovskite devices. *Energy Environ. Sci.* **2018**, *11*, 629–640.
- (67) Blakesley, J. C.; Castro, F. A.; Kylberg, W.; Dibb, G. F. A.; Arantes, C.; Valaski, R.; Cremona, M.; Kim, J. S.; Kim, J.-S. Towards reliable charge-mobility benchmark measurements for organic semiconductors. *Org. Electron.* **2014**, *15*, 1263–1272.
- (68) Luck, K. A.; Sangwan, V. K.; Hartnett, P. E.; Arnold, H. N.; Wasielewski, M. R.; Marks, T. J.; Hersam, M. C. Correlated In Situ Low-Frequency Noise and Impedance Spectroscopy Reveal Recombination Dynamics in Organic Solar Cells Using Fullerene and Non-Fullerene Acceptors. *Adv. Funct. Mater.* **2017**, *27*, 1703805.
- (69) Sangwan, V. K.; Zhu, M.; Clark, S.; Luck, K. A.; Marks, T. J.; Kanatzidis, M. G.; Hersam, M. C. Low-Frequency Carrier Kinetics in Perovskite Solar Cells. *ACS Appl. Mater. Interfaces* **2019**, *11*, 14166–14174.
- (70) Yan, C.; Barlow, S.; Wang, Z.; Yan, H.; Jen, A. K. Y.; Marder, S. R.; Zhan, X. Non-fullerene acceptors for organic solar cells. *Nat. Rev. Mater.* **2018**, *3*, 18003.
- (71) Garcia-Belmonte, G.; Boix, P. P.; Bisquert, J.; Sessolo, M.; Bolink, H. J. Simultaneous determination of carrier lifetime and electron density-of-states in P3HT:PCBM organic solar cells under illumination by impedance spectroscopy. *Sol. Energy Mater. Sol. Cells* **2010**, *94*, 366–375.
- (72) Xu, L.; Wang, J.; Lee, Y.-J.; Hsu, J. W. P. Relating Nongeminate Recombination to Charge-Transfer States in Bulk Heterojunction Organic Photovoltaic Devices. *J. Phys. Chem. C* **2015**, *119*, 19628–19633.
- (73) Basham, J. I.; Jackson, T. N.; Gundlach, D. J. Predicting the J–V Curve in Organic Photovoltaics Using Impedance Spectroscopy. *Adv. Energy Mater.* **2014**, *4*, 1400499.
- (74) Heiber, M. C.; Okubo, T.; Ko, S. J.; Luginbuhl, B. R.; Ran, N. A.; Wang, M.; Wang, H. B.; Uddin, M. A.; Woo, H. Y.; Bazan, G. C.; Nguyen, T. Q. Measuring the competition between bimolecular charge recombination and charge transport in organic solar cells under operating conditions. *Energy Environ. Sci.* **2018**, *11*, 3019–3032.
- (75) Stolterfoht, M.; Armin, A.; Philippa, B.; White, R. D.; Burn, P. L.; Meredith, P.; Jüka, G.; Pivrikas, A. Photocarrier drift distance in organic solar cells and photodetectors. *Sci. Rep.* **2015**, *5*, 9949.